Journal of Molecular Structure 1340 (2025) 142452

Contents lists available at ScienceDirect

Journal of Molecular Structure

journal homepage: www.elsevier.com/locate/molstr

$Ca_{0.89}Tm_{0.007}Ho_{0.003}Yb_{0.1}MoO_4$ phosphor for nonthermally coupled level-based temperature sensing and latent fingerprint detection

Sachin Singh, Pradeep K. Vishwakarma, Manisha Sharma, Sunil K. Singh *

Department of Physics, Indian Institute of Technology (BHU), Varanasi, Uttar Pradesh, 221005, India

ARTICLE INFO

Keywords:
Optical properties
Lanthanide
Energy transfer
LFPs
NTCLs
Temperature sensing

ABSTRACT

This study explores the spectral feature of Ln^{3+} (Ho^{3+}, Tm^{3+}, Yb^{3+}) doped $CaMoO_4$ phosphor for non-thermally coupled levels (NTCLs) based temperature sensing and latent fingerprints (LFPs) detection. Phase analysis of hydrothermally synthesized $CaMoO_4$:Ln^{3+} phosphors, reveals the formation of tetragonal lattice with $I4_1/a$ space group. An increment in particle size has been observed due to modification caused by doping of Ho^{3+}/Tm^{3+}/Yb^{3+} ions. Fourier transform infrared spectroscopy (FTIR) study corroborates the desired lattice formation, while UV–Vis analysis indicates a significant reduction in optical bandgap after incorporating Ln^{3+}in the $CaMoO_4$. Optical properties of Ho^{3+} and Tm^{3+} ions, individually or in combination with Yb^{3+} ions, demonstrate strong Upconversion (UC) emission spanning the visible region. Temperature-dependent emission of Ho^{3+}/Tm^{3+} is employed for temperature sensing based on NTCLs fitted by Boltzmann sigmoidal function, which reveals the maximum temperature sensitivity for the I_{795}/I_{473} (69.86×10^{-2} K^{-1} at 500 K). In addition, the luminescent phosphor materials have also been demonstrated for LFP detection through the powder dusting technique. Conclusively, these phosphor materials show multifunctionality and great potential for optical applications.

1. Introduction

In recent decades, the significant strides have been made in the development of versatile advanced phosphors materials for application in the high-precision temperature sensing and LFPs detection. Ln^{3+}-doped phosphors exhibit distinctive optical characteristics, including sharp spectral bands, dual-mode photoconversion, charge transfer bands, cascaded energy transfer, quantum cutting, colour tunability, photo avalanche, facilitating their application across multiple fields, notably display devices, anti-counterfeiting, optoelectronics, data storage, bio-imaging, optical temperature sensing, etc. [1–5]. Temperature is the most fundamental physical parameter, and their precise measurement is crucial for scientific study, metallurgy, electronics, industries, biological sciences, and other fields. Conventional temperature sensing typically utilises Resistance Temperature Detectors (RTDs), thermocouples, and thermistors, which necessitate direct physical contact with the materials being measured [6,7]. In converse, the growing recognition of optical thermometry mitigates the constraints of electrical resistance and can be ascribed to temperature-dependent optical properties, including emission intensity, fluorescence lifetime, fluorescence intensity ratio (FIR), peak position, and polarization anisotropy, as temperature-dependent variables. Additionally, it offers rapid response, exceptional sensitivity, and ability to measure minute, dynamic, or inaccessible objects [8,9]. Furthermore, the trouble with the inevitable influx of stray light and background autofluorescence for some substances under investigation, could be rectified using UC materials.

Researchers mostly emphasize the FIR methodology for optical temperature sensing, wherein the emission from thermally coupled levels (TCLs) is measured as a function of temperature, with the FIR trend following the Maxwell-Boltzmann distribution law [10,11]. Nevertheless, this approach encounters notable challenges, including slow response time, limited sensitivity, non-linearity constraints, energy gap fluctuations and in certain instances, inadequate spectral resolution [12]. In contrast, emission acquired from NTCLs has emerged as a transformative approach in optical thermometry, offering substantial advantages over the TCLs method and serving as a promising alternative [13]. The NTCLs approach harnesses emission for FIR from either the same or different activators, delivering improved sensitivity and operational flexibility over a broad range of temperature conditions, while ensuring consistent performance without constraints of energy gap fluctuations [13,14]. This approach entails fitting the NTCLs-based FIR

* Corresponding author.
E-mail address: sunilks.app@itbhu.ac.in (S.K. Singh).

https://doi.org/10.1016/j.molstruc.2025.142452
Received 6 February 2025; Received in revised form 9 April 2025; Accepted 20 April 2025
Available online 21 April 2025

to a mathematical model and calculating parameters such as relative sensitivity (S_r) and absolute sensitivity (S_a) for comparative analysis. A key advantage of NTCL-based thermometry is its ability to achieve significantly higher temperature sensitivities, often exceeding 10 % K^{-1}, while also reducing temperature uncertainty and improving signal discrimination. Furthermore, NTCLs enable a broader operational temperature range and superior signal recognition, making them particularly suitable for applications in extreme environments and micro-temperature sensing [15]. An emerging application of Ln^{3+}-activated phosphors is in LFPs detection, a key tool in forensic investigations that aids in identifying individuals by revealing unique ridge patterns left on various surfaces. Conventional techniques typically rely on powders or chemical reagents, which are constrained by environmental conditions and substrate compatibility, whereas Ln^{3+} phosphors offer a more reliable and effective method, enhancing fingerprint visibility and contrast across diverse backgrounds and colours [16].

Employing economical and reliable host materials, suitable dopant ions, and an appropriate synthesis approach is vital for achieving intense and consistent emission. In this context, $CaMoO_4$, an inorganic host with exceptional chemical and physical properties, demonstrates excellent thermal stability, optical transparency, low phonon energy, efficient incorporation of foreign elements (particularly La^{3+} ions), and a wide bandgap (3.7–5 eV) that reduces energy loss and prevents non-radiative recombination [17–19]. These attributes enhance its optical properties, making it a promising choice for luminous material hosts over other oxide-based phosphors for higher sensitive thermometry. $CaMoO_4$ belongs to the scheelite family and has a tetragonal structure classified $I4_1/a$ space group. The crystalline structure of $CaMoO_4$ features a MoO_4 tetrahedron linked to a dodecahedral (CaO_8) unit through shared vertices, with Ca ions serving as potential sites for substitution through Ln^{3+} doping [19]. As luminescent centres, the Ho^{3+} ions is recognized for its intense green ($^5F_4$, $^5S_2 \rightarrow {}^5I_8$), red ($^5F_5 \rightarrow {}^5I_8$), and weak NIR ($^5F_4$, $^5S_2 \rightarrow {}^5I_7$) emission, with the $^5F_4/^5S_2$ levels serves as TCLs, as documented by multiple investigations; nonetheless, the energy gap ($\Delta E \sim 250\ cm^{-1}$) between these levels exhibits limited spectral resolution [20, 21]. In contrast, Tm^{3+} ions exhibit strong blue ($^1G_4 \rightarrow {}^3H_6$) and NIR ($^3H_4 \rightarrow {}^3H_6$) regions, along with temperature-dependent thermally coupled emission in the red region ($^3F_{2,3}$ and $^3H_4 \rightarrow {}^3H_6$). Meanwhile, Yb^{3+} ions ($^2F_{5/2} \rightarrow {}^2F_{7/2}$) function as sensitizers, efficiently transferring energy to both Ho^{3+} and Tm^{3+} ions in UC process [21]. In recent, various researchers has highlighted the temperature-sensing potential of $CaMoO_4$ doped with different lanthanide ions. Sinha et al. reported an enhanced sensitivity of 0.0216 K^{-1} at 490 K in $CaMoO_4$: Er^{3+}/Yb^{3+} and K^+/Na^+ as foreign element, employing the thermally coupled levels ($^2H_{11/2}$ and $^4S_{3/2}$) of Er^{3+} [22]. Similarly, Gouraha et al. found dual temperature sensitivity in $CaMoO_4$: Er^{3+}/Yb^{3+}, reporting a maximum absolute sensitivity of $10.74 \times 10^{-3}\ K^{-1}$ at 500 K [23]. Dey and Rai further investigated $CaMoO_4$: $Er^{3+}/Tm^{3+}/Yb^{3+}$, achieving a sensitivity of $0.0182\ K^{-1}$ at 413 K and emphasizing its optical heating properties [24]. In our previous work, we compared the temperature-sensing properties of bulk and nanoparticle forms of $CaMoO_4$:Er^{3+}/Yb^{3+} phosphors [25]. In a subsequent study, we introduced a third dopant as Bi^{3+} ions, and their impact on UC behaviour and optical temperature sensitivity [10]. However, to the best of our knowledge, this host has not yet been explored for NTCLs-based optical thermometry so far.

This study primarily aims to synthesize $CaMoO_4$ phosphors doped with Ho/Yb, Tm/Yb, and Ho/Tm/Yb using hydrothermal approach, followed by high-temperature sintering to enhance their structural and optical properties. The phase formation, morphology, optical absorption and associated vibrational modes of the host have been thoroughly investigated using XRD, SEM, UV–Vis and FTIR techniques. The optical characteristics of the synthesized materials were examined under NIR excitation (λ_{exci} = 980 nm), along with a comprehensive power-dependent emission analysis to evaluate the involvement of a number of photons for a particular UC transition. Temperature sensing properties are determined by evaluating temperature-dependent UC measurements between 300 and 572 K. Whereas "powder dusting approach" was employed to generate LPFs left on a glass slide, and a camera equipped with a particular filter was used to record the results under NIR illumination.

2. Experimental section

2.1. Synthesis procedure

All phosphor samples were synthesized using a facile hydrothermal treatment at 180 °C, subsequently followed by calcination at 750 °C to enhance crystallinity [26]. The starting AR grade precursors, Ca $(NO_3)_2{\cdot}4H_2O$ (98 %), $(NH_4)_6Mo_7O_{24}{\cdot}4H_2O$ (99.0 %). In contrast, the lanthanides dopants i.e., Ho_2O_3 (99.9 %), Tm_2O_3 (99.99 %) and Yb_2O_3 (99.99 %) were obtained from Alfa Aesar. All the chemicals were used without any further post-treatment. Initially, the REs oxides were dissolved in a dilute nitric acid (Fisher Scientific) at 80 °C to convert them into metal nitrates chemically. After this, these metal nitrates were washed 2–3 times in doubly deionized water to remove the nitric acid traces. Now, the 5 ml aqueous solution of REs nitrates in deionized water was prepared in beakers separately for further use.

As in a typical hydrothermal process, the water-soluble stochiometric amounts of precursors for different samples were dissolved in deionized water, preheated at 80 °C and vigorously stirred for 2 h to get the uniform solution. Now, the whole solution was poured into an autoclave and kept at a temperature of 140 °C for hydrothermal treatment for 24 h. After cooling down the autoclave to room temperature, the samples were collected by centrifugation and washed 2–3 times using ethanol and water. A white powder sample is then obtained and placed for post-treatment at 750 °C for 3 h to improve crystallinity. A similar synthesis method is adopted for each sample. The optimized doubly and triply doped phosphor samples with its doping concentrations are designated as $CaMoO_4$:Ho^{3+}/Yb^{3+} ($Ca_{0.897}Ho_{0.003}Yb_{0.1}MoO_4$), $CaMoO_4$:Tm^{3+}/Yb^{3+} ($Ca_{0.893}Tm_{0.007}Yb_{0.1}MoO_4$), and $CaMoO_4$:$Ho^{3+}/Tm^{3+}/Yb^{3+}$ ($Ca_{0.89}Tm_{0.007}Ho_{0.003}Yb_{0.1}MoO_4$) phosphors.

2.2. Materials characterization

The X-ray diffraction (XRD) patterns of the samples were recorded (10°−80°, step size 0.01°) using a Rigaku Miniflex 600 X-ray diffractometer, employing Cu Kα X-ray radiation source of 1.54 Å wavelength. Surface morphology and elemental composition of the phosphors were evaluated through field-emission scanning electron microscopy (FE-SEM) using Nova Nano SEM 450, USA setup. Particle size and compositional analysis were done through the acquisition of Transmission Electron Microscope (TEM) images using a Tecnai G2 20 TWIN 200 kV (FEI) system. Analysis of the existing vibrational group within the 400–4000 cm^{-1} range in materials was monitored by FTIR spectrometer (Nicolet iS5), while the Shimadzu UV-2600 spectrophotometer was employed to analyse the materials' specific absorbance in UV–visible-NIR spectral range (200–1200 nm) and to analyse the band gap variation. Horiba fluorolog-3 spectrophotometer equipped with 450 W Xenon lamp and PMT detector was used to record the room temperature and power-dependent UC spectra of prepared samples using a 980 nm diode-laser as excitation source, while an indigenous heater setup was used for temperature variation above room temperature. UC lifetime was assessed using a setup comprising a 980 nm diode laser modulated by a mechanical chopper (model no SR-540, Stanford Research Systems Inc.) as the excitation source and a photomultiplier tube (PMT) coupled with a monochromator as the signal detector, and a 150 MHz oscilloscope (model no HM 1507, Hameg Instruments) connected to a computer for displaying the decay curve. The visualization of coloured LFPs is carried out through the 'Powder Dusting Approach,' where the powder is applied on a LFPs leftover glass substrate, and images are captured using various filters under NIR excitation.

3. Result and discussions

3.1. Phase, particle shape/size, and elemental mapping analysis

X-ray diffraction measurements were carried out to determine the phase and crystalline structure of the phosphor samples calcinated at 750 °C. The optimized doubly and triply doped phosphor samples are designated as $CaMoO_4$:Ho^{3+}/Yb^{3+} (CMOHY), $CaMoO_4$:Tm^{3+}/Yb^{3+} (CMOTY), and $CaMoO_4$:Ho^{3+}/Tm^{3+}/Yb^{3+} (CMOHTY) phosphors, respectively, for their respective demonstrations. The XRD patterns of the pristine CMO, as well as the optimized samples CMOHY, CMOTY, and CMOHTY, reveal the formation of a scheelite-type tetragonal structure with I 4_1/a space group [JCPDS: 29–0351] and T_d symmetry [19]. Fig. 1(a) depicts the diffraction patterns of phosphor samples, which align with previously reported data, substantiating well formation of the calcium molybdate framework [10]. While the absence of impurity peaks signifies the successful incorporation of Ho^{3+} (1.015 Å)/ Tm^{3+} (0.994 Å) /Yb^{3+} (0.985 Å) in the CMO lattice. Despite the disparity in valency between Ca^{2+} (1.12 Å) and Ln^{3+} dopant ions, the proximity of ionic radii, charge compensation mechanisms (such as defect or oxygen vacancy formation), and also crystal structure flexibility, facilitates successful doping without disrupting the lattice. Furthermore, the low concentration of dopants prevents the crystal from exhibiting any significant charge imbalance in the crystal lattice [27, 28]. The crystalline structure of $CaMoO_4$ consists of a tetrahedron of MoO_4 connected to a dodecahedron (CaO_8) at shared vertices, as seen in the Fig. 1(b).

The average crystallite sizes of the CMO, CMOHY, CMOTY, and CMOHTY samples are calculated using the Debye-Scherrer equation [29]:

$$D = \frac{0.89\lambda}{\beta cos\theta} \quad (1)$$

Here, D represents the average crystallite size, λ (1.54 Å) denotes the wavelength of the used X-rays, and β signifies the full width at half maximum (FWHM) of diffraction peaks. The estimated average crystallite sizes for CMO, CMOHY, CMOTY, and CMOHTY are 54 nm, 58 nm, 64 nm, and 72 nm, respectively. Thus, the optimized lanthanide doping causes an enhancement in the crystallite size, which also owe to improved optical characteristics. Furthermore, the indirect approach for estimating dislocation density (δ) [30]:

$$\delta = \frac{1}{D^2} \quad (2)$$

Here, D is the estimated crystallite size facilitates the initial evaluation of crystallographic defects or irregularities. The determined dislocation densities of CMO, CMOHY, CMOTY and CMOHTY are 34.29×10^{13} m^{-2}, 29.72×10^{13} m^{-2}, 24.41×10^{13} m^{-2}, and 19.29×10^{13} m^{-2}, respectively. The reducing dislocation densities with lanthanide doping signifies the reduction in defect and also would lead to enhanced optical properties [31].

Moreover, Rietveld refinement of the developed phosphor samples has been accomplished using the 'Fullprof Suite' (5.10) program, employing the XRD data as initial parameters for evaluating the lattice parameters [32]. The Pseudo-Voigt peak shape function was used to fit the diffraction peaks, while a linear interpolation function with refinable heights was employed as the background function. Fig. 2 depicts the refinement plots along with goodness of fitting, whilst Table 1 summarizes the structural parameters and residuals of the refinement. The structural refinement further corroborates the establishment of tetragonal phase with I 41/a space group, and denied the presence of impurities peaks. This similarity can be attributed to the comparable ionic radii of the dopant ions (Ho^{3+}, Tm^{3+}, and Yb^{3+}) with the Ca^{2+} ion. As a result, it is possible to conclude that different Ln^{3+} were successfully incorporated into the pure $CaMoO_4$ sample.

Morphological assessments of developed phosphor samples were performed by SEM image analysis taken at various resolutions. The SEM images of CMO phosphors reveal mostly agglomerated, distorted

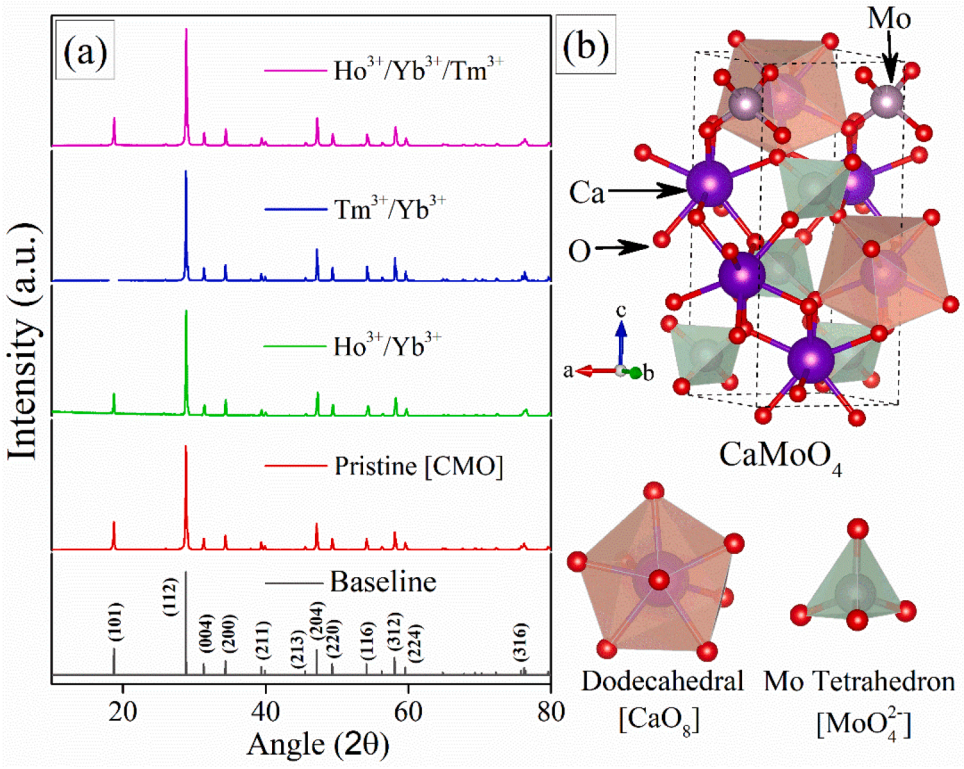

Fig. 1. (a) X-ray diffraction patterns of pristine CMO, CMOHY, CMOTY, and CMOHTY phosphors materials calcined at 750 °C, (b) Tetragonal crystalline lattice of $CaMoO_4$.

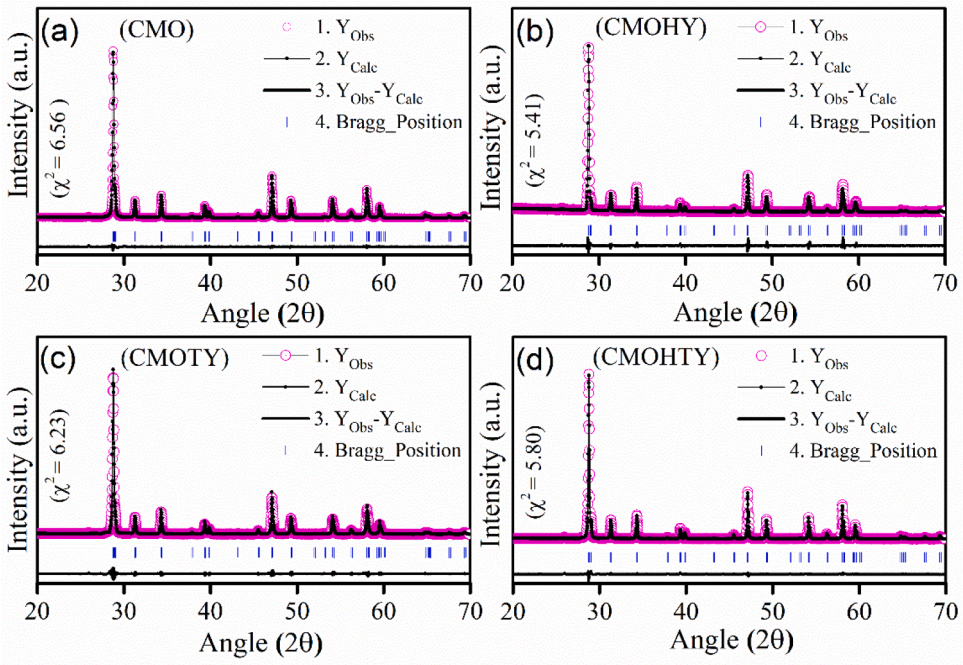

Fig. 2. Rietveld refinement of XRD plots of CMO, CMOHY, CMOTY, and CMOHTY phosphors.

Table 1
List of refined structural parameters and residuals of refinements of four different powder samples: CMO, CMOHY, CMOTY, and CMOTHY, as determined by Rietveld analysis.

Sample		CMO	CMOHY	CMOTY	CMOHTY
	Peak Shape Function: Pseudo-Voigt, ***Phase Structure:*** Tetragonal [$I4_1/a$ (88)]				
Lattice Parameters	$a = b$ (Å)	5.22683±4 × 10^{-5}	5.2231±1.5 × 10^{-4}	5.2246±4 × 10^{-5}	5.2278±3 × 10^{-5}
	c (Å)	11.44157±1.5 × 10^{-4}	11.4108±4.5 × 10^{-4}	11.4332±1.5 × 10^{-4}	11.4287±1.1 × 10^{-4}
	α = β = γ=90				
	Volume ($Å^3$)	312.580±5 × 10^{-3}	311.301±1.8 × 10^{-2}	312.086±5 × 10^{-3}	312.355±4 × 10^{-3}
	Density (g/cm^3)	4.250	5.083	5.091	5.126
Residuals of Refinement	R_p (%)	4.12	8.24	6.86	3.80
	R_{wp} (%)	5.75	11.4	9.16	5.35
	R_{exp} (%)	2.25	4.90	2.21	2.22
	χ^2 (%)	6.56	5.41	6.23	5.80

spherical forms with an average particle size of approximately 185 nm, as seen in Fig. 3(a). Particle distribution plots are provided in the insets of each SEM image. Doping of Ho^{3+}/Yb^{3+} ions in the CMO lattice results in a partially refined spherical morphology with an average particle dimension of around 400 nm, whereas the incorporation of Tm^{3+}/Yb^{3+} ions yields almost spherical morphology with an average particle size of around 800 nm, as seen in Fig. 3(b-c). Furthermore, the tri-doped ($Ho^{3+}/Tm^{3+}/Yb^{3+}$) CMO phosphor intriguingly acquired an oval morphology with varied dimensions, averaging 1500 nm in length, as seen in Fig. 3(d). Dopants significantly affect the growth kinetics of particles, resulting in morphological changes that enhance the propensity for agglomeration. Specifically, the heteromorphic substitution of Ca^{2+} ions with rare earth elements such as Ho^{3+}, Tm^{3+}, or Yb^{3+} introduces interstitial oxygen vacancies. These vacancies can facilitate the agglomeration of particles, resulting in refined structures that exhibit spherical or oval shape structures [33,34]. It is worth noting that an increase in crystallite and particle size may contribute to improved optical properties. The elemental analysis of phosphor samples using EDAX spectra concurrently reflects the incorporation of different lanthanide ions (shown in bottom of each SEM images), which distinctly indicates the presence of Ca, Mo, and O (host constituents), together with traces of the doped elements Ho, Tm, and Yb.

Selected area EDS mapping (elemental mapping) of CMOHTY phosphors further corroborates the homogeneous elemental distribution over the sample's surface, as seen in Fig. 4. Weight percentage of each element in CMOHTY is also listed in the Fig. 4. TEM images of CMOHTY phosphors calcined at 750 °C, depicted in Fig. 5(a-b), reveal the actual rutile shape of the particles throughout various distribution ranges. The interference fringe pattern caused by a fundamental lattice plane (112) having an interplanar spacing (d-value) of 2.19 Å is seen in Fig. 5(c). Furthermore, the SAED patterns exhibited distinct dotted ring formations, indicating that the developed phosphors were mainly polycrystalline as displayed in Fig. 5(d) [35]. The prominent diffuse ring in the pattern is overlaid on a singular sharp point, with the brightest diffraction ring matching to the (112) diffraction plane of $CaMoO_4$ lattice.

3.2. *Vibrational mode analysis*

Developed samples were also examined by FTIR to evaluate the existing vibrational modes in the phosphor samples. Fig. 6 displays the FTIR spectra of CMO, CMOHY, CMOTY, and CMOTHY recorded in transmittance mode within the range of 400–4000 cm^{-1}. The prominent vibrational band in pristine CMO as well as doped CMO samples display the bands occurring at around 428, 812, 1629 and 3459 cm^{-1}. The most significant vibrational bands in pure CMO and doped samples occur at around 428 cm^{-1} and 812 cm^{-1}, indicating the formation of a $CaMoO_4$ lattice [10,17]. The band appearing at 428 cm^{-1} is attributed to bending

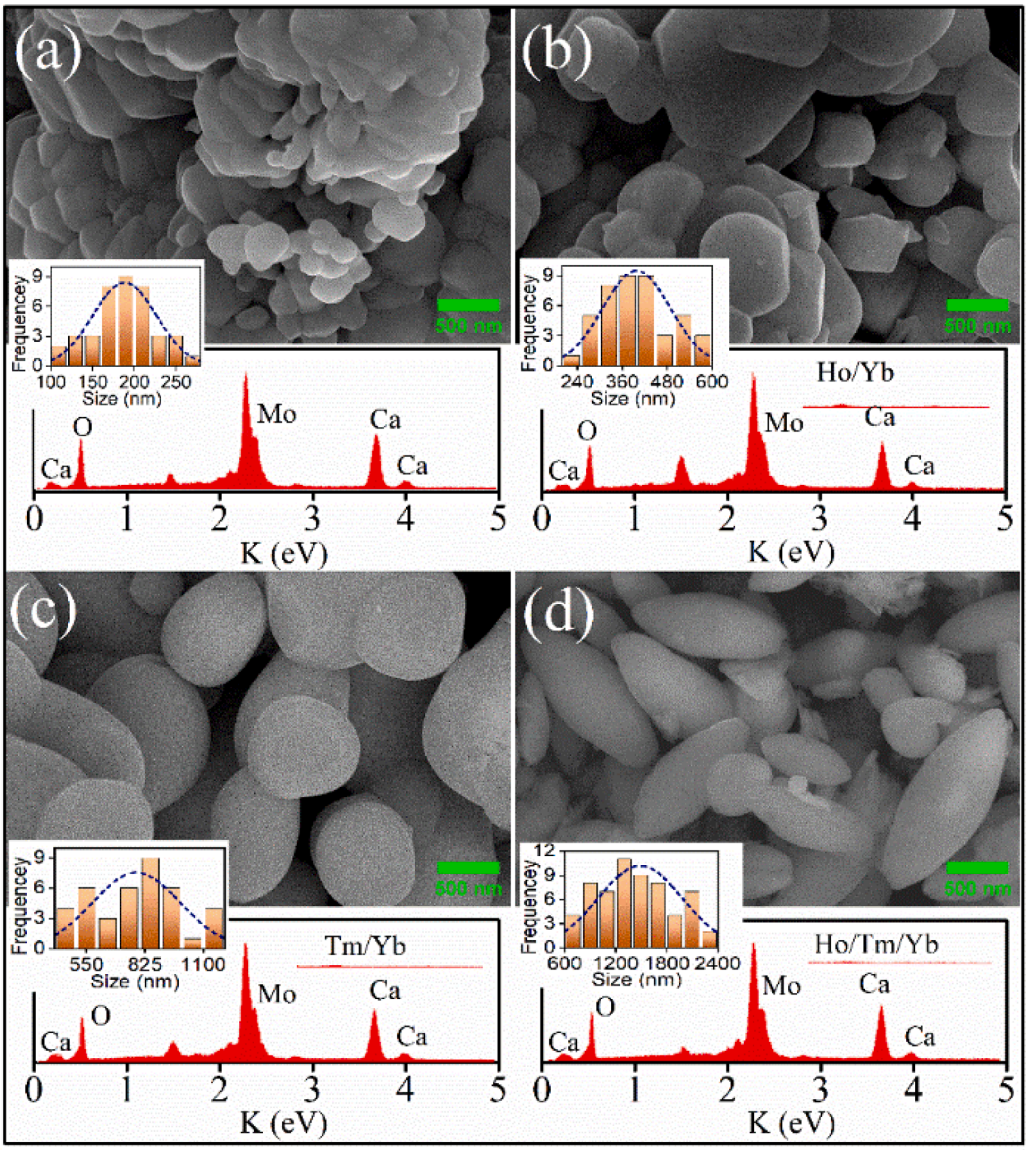

Fig. 3. SEM images of (a) CMO, (b) CMOHY, (c) CMOTY, and (d) CMOHTY phosphors sample along with EDAX analysis (in bottom of respective micrograph) with particle size distribution plots (as inset).

vibration of Mo-O bond present in the MoO_4^{2-} tetrahedron, whereas the strong depth band at 812 cm^{-1} is arising due to anti-symmetric vibration of O-Mo-O present in the MoO_4^{2-} complex [36]. This suggests tetrahedral coordination of molybdenum atoms, resulting in a four-sided pyramid containing oxygen atoms at its vertices. In addition, the bands at 1629 cm^{-1} (H—O-H bending) and 3459 cm^{-1} (O—H stretching) are attributed to absorbed H_2O molecules to the lattice, demonstrating a slightly hygroscopic nature of the sample [36].

3.3. UV–visible-NIR absorption and bandgap analysis

The UV–Vis absorption spectra in reflectance mode were employed to figure out the host absorption and the dopant optical characteristics in pristine CMO and three other doped samples, i.e., CMOHY, CMOTY and CMOHTY. Fig. 7(a) depicts the UV–Vis spectra of the CMO host, representing the band absorbance between 200 and 400 nm due to the optical absorption of the molybdate tetrahedron (MoO_4^{2-}) group [25]. Additionally, the modest dopant concentration of Ln^{3+} (Ho^{3+}/Tm^{3+}/Yb^{3+}) still appears with reasonable intensity, verifying their presence and exhibiting considerable excitation bands. The absorbance band appeared in the visible region at 454 nm, 541 nm and 644 nm, corresponding to $^5I_8 \rightarrow {}^5G_6$, $^5I_8 \rightarrow {}^5F_4$ ($^5S_2$) and $^5I_8 \rightarrow {}^5F_5$ intrinsic electronic transition, respectively, attributed to intrinsic Ho^{3+} ions absorption [32]. While the absorbance bands situated at 688 nm and 795 nm, which are related to $^1G_4 \rightarrow {}^3F_{2,3}$ and $^3H_6 \rightarrow {}^3H_4$ electronic transition, correspond to intrinsic Tm^{3+} ions absorption. Furthermore, the Yb^{3+} ions absorption bands at 976 nm ($^2F_{7/2} \rightarrow {}^2F_{5/2}$) were used to establish the UC spectra [15,37].

In pristine CMO, an absorption cut edge is noted near 300 nm, aligning with its bandgap, which shifts in more UV region by nearly 10 nm following doping of Ln^{3+} ions, clearly signifying a reduction in the optical bandgap. Tauc plots [$(\alpha h\nu)^2$ vs $h\nu$], seen in Fig. 7(b), are employed to ascertain the bandgap (E_g) of the phosphors samples [38]. The pristine CMO sample demonstrates an obvious band gap of approximately 4.88 eV, while a significant decrease in the band gap is noted upon Ln^{3+} doping. The optical bandgap of the CMOHY, CMOTY, and CMOHTY phosphor samples is around 3.96 eV, 3.93 eV, and 3.99 eV, respectively. The discrepancies observed in the optical bandgap (E_g) values between doped and undoped phosphors can be attributed to the introduction of localised energy states within the bandgap, the ionic size of the dopants, and the charge compensation mechanisms that enable the emergence of vacancies, defects or disorder, particularly as a result

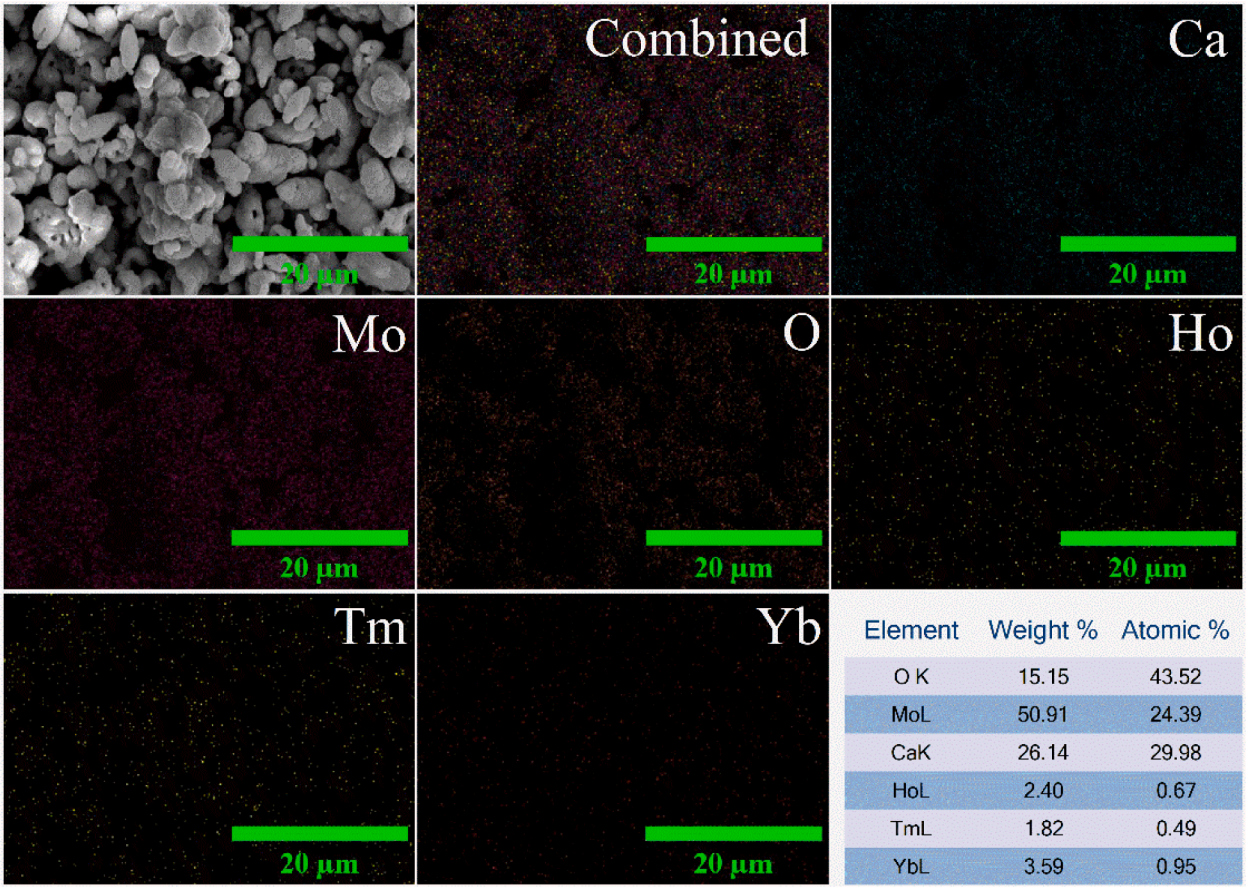

Element	Weight %	Atomic %
O K	15.15	43.52
MoL	50.91	24.39
CaK	26.14	29.98
HoL	2.40	0.67
TmL	1.82	0.49
YbL	3.59	0.95

Fig. 4. Elemental mapping of a selected region of the CMOHTY phosphor sample.

of the substitution of Ca^{2+} by Ln^{3+} ions [37]. The defects or vacancies resulting from Ln^{3+} (Ho^{3+}, Tm^{3+}, and Yb^{3+}) doping establish a significant potential gradient within the host matrix. This gradient leads to the quantum mechanical penetration of localised states into the forbidden band gap. These states can also serve as charge carrier recombination sites, thereby reducing the energy difference between the conduction and valence bands [39,40].

3.4. Infrared to visible up-conversion emission analysis

The photon up-conversion process in Ho^{3+} ions is widely recognized for its emission in the green and red regions of the EM spectrum; nevertheless, its emission efficiency is primarily influenced by the host's crystallographic asymmetry, morphology, particle size, and also foreign dopants, among other factors. Moreover, the dominance of the particular band's emission is attributed to the phonon frequency. Doping Ho^{3+}/Yb^{3+} (in mol %) in $CaMoO_4$ yields dazzling green emitting bands at 545 nm, as well as relatively small red (655 nm) and NIR emission (755 nm) bands under 980 nm excitation, which spans the mid-visible region as shown in Fig. 8. Intense green emission of Ho^{3+} ions is attributed to the $^5S_2/^5F_4 \rightarrow {}^5I_8$. In contrast, the red and NIR emission is due to the $^5F_5 \rightarrow {}^5I_8$ and $^5S_2/^5F_4 \rightarrow {}^5I_7$ electronic transitions, respectively [32]. Through experimental exploration, the ideal concentration of Ho^{3+} ions for optimal UC performance is determined to be approximately 0.3 mol %, with Yb^{3+} ions held constant at 10 mol %. This configuration is designated as CMOHY phosphors. However, increasing the Ho^{3+} concentration beyond this point leads to concentration quenching, resulting in diminished emission when subjected to near-infrared (NIR) excitation [39–41].

Meanwhile, precisely Tm^{3+}/Yb^{3+} doping, referred to as CMOTY, emits in the blue (473 nm) and NIR (795 nm) regions of the EM spectrum, ascribed to $^1G_4 \rightarrow {}^3H_6$ and $^1F_2 \rightarrow {}^3H_6$ ($^3H_4 \rightarrow {}^3H_6$) electronic transitions, respectively [24,37]. Numerous studies indicate that the optimal doping concentration for Tm^{3+} ions typically ranges from 0.5 to 1 mol % [42]. In this context, the ideal concentration of Tm^{3+} in $CaMoO_4$ has been identified as 0.7 mol %, with Yb^{3+} ions consistently held at 10 mol %. The goal is to harness temperature-sensing properties derived from the NTCLs of doped Ln^{3+} ions. Doping of Ho^{3+}/Tm^{3+} encompasses multiple emitting bands covering the visible range, allowing for selecting a distinct set of emitting bands. Therefore, an integrated Ho^{3+}/Tm^{3+} doped phosphor with two optically active centres is employed to harvest the emission characteristics, referred to as CMOHTY. Now, we have four emitting bands corresponding to Ho^{3+} and Tm^{3+} ions emission, showing the temperature-dependent behaviour, which is further employed to study the temperature sensing application.

An analysis of power-dependent UC emission intensity has been performed to ascertain the number of photons engaged in the UC process in the CMOHTY phosphor sample. Power-dependent UC is determined using the equation ($I_{up} \; \alpha \; P^n$), where I_{up} is integrated intensity, P is excitation power, and n is the number of photons needed to reach the emission level [25]. It shows that almost two NIR photons are involved in getting green and red UC emissions [~1.81 (green) and ~1.71 (red)] from Ho^{3+} ions, which is reasonable for the UC emission mechanism. For Tm^{3+} ion, UC emission exhibited almost 3 photons for blue emission and 1.5 photons for red emission. The reasonable UC emission mechanism for both Ho^{3+} and Tm^{3+} ions can be seen in the energy level diagram (Fig. 9).

Investigating the decay times across different emission bands of Ho^{3+} and Tm^{3+} ions under 980 nm excitation reveals single exponential function fitting of decay profile. This suggests a singular pathway for population build up in the excited states of both ions. Lifetime of each state, is determined by fitting the decay curve to a single exponential

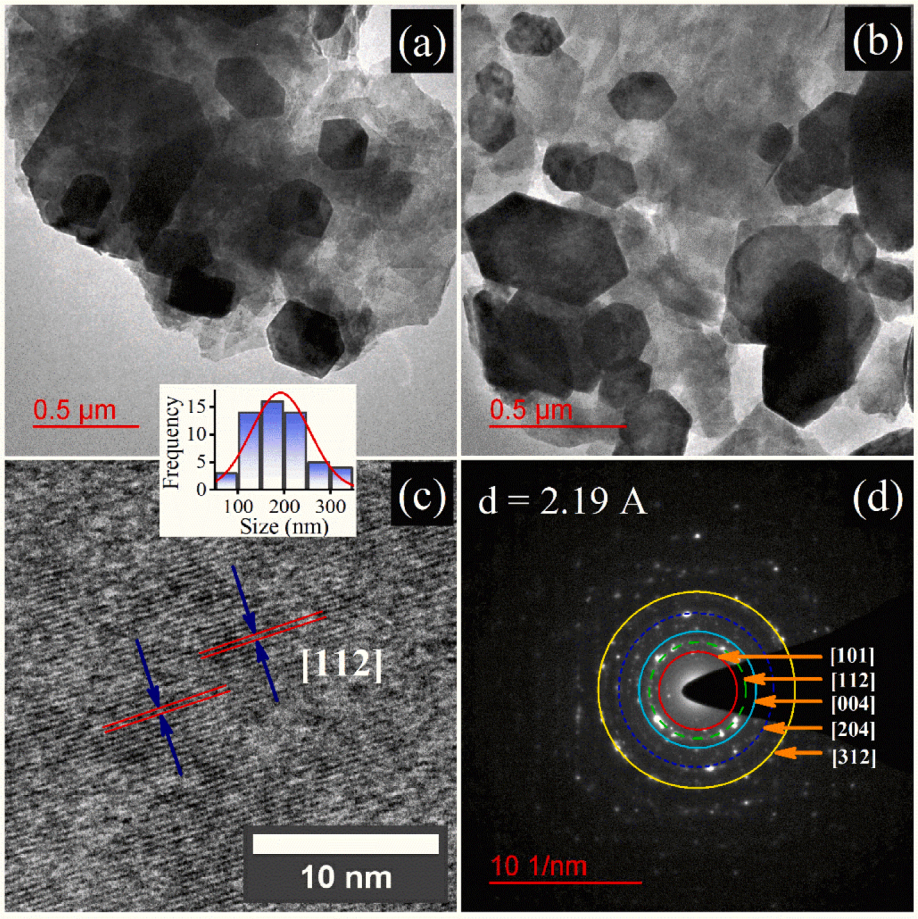

Fig. 5. (a-b) TEM images of optimized CMOHTY phosphors at varying resolutions, (c) Interference fringes of the [112] lattice plane, (d) SAED pattern.

function, expressed as $I=I_o \exp(-t/\tau)$, where τ denotes the lifetime of the state [32]. Fig. 10 presents the fitted decay curves for the key emitting states associated with Ho^{3+} and Tm^{3+} ions in the CMOHY, CMOTY, and CMOHTY phosphor samples under 980 nm excitation, accompanied by a detailed analysis. Notably, the lifetimes of the green ($^5F_4/^5S_2$) and red ($^5F_5$) emission states of Ho^{3+} in CMOHTY exhibit a slight enhancement relative to those in CMOHY. Conversely, the Tm^{3+} emission states at 473 nm ($^1G_4 \rightarrow {}^3H_6$) and 795 nm ($^3H_4 \rightarrow {}^3H_6$) demonstrate a pronounced reduction in lifetime in CMOHTY when compared to CMOTY. The marked reduction in the lifetime of Tm^{3+} is primarily attributed to energy transfer to Ho^{3+} ions, providing strong evidence for the interaction between Tm^{3+} and Ho^{3+}, as reported by Liu et al. [43]. This interaction is facilitated through energy transfer pathways originating from the excited $^1G_4$ state of Tm^{3+} ions to the green-emitting $^5F_4/^5S_2$ state of Ho^{3+} ions [44]. Additionally, Huang et al. reported that the energy transfer is likely due to an enhanced rate of two cross-relaxation processes between Tm^{3+} and Ho^{3+} ions at elevated Tm^{3+} doping concentrations, which accelerates the radiative relaxation processes of Ho^{3+} ions involving $^5S_2/^5I_8$ and $^5F_5/^5I_8$ transitions [41].

4. Multifunctional behaviour of CMOHTY phosphor

4.1. Temperature sensing application

An assessment of the temperature sensing potential of the developed phosphor materials, i.e., $CaMoO_4$:$Ho^{3+}/Tm^{3+}/Yb^{3+}$ (CMOTHY), is carried out by tracking the fluorescence intensity emitted by doped Ln^{3+} ions with a variation of external temperature. For this purpose, the FIR of different emission bands that respond well to temperature is calculated. There exists a varying degree of temperature-dependent response in the emission bands of Tm^{3+} (473 nm, 795 nm) and Ho^{3+} (545 nm, 655 nm), with an apparent decrease in emission intensity as temperature increases as shown in Fig. 11. In general, the chance of non-radiative transition is dominated with the rise of temperature, hence the emission intensity reduces, which is usually referred as temperature quenching phenomenon [44]. In some instances, the emission intensity initially exhibits an upward trend in low-temperature constraints; whereas, as the temperature nears a critical threshold, non-radiative relaxation begins to predominate with an additional increase in temperature, attributable to the relative competition between non-radiative relaxation and temperature quenching effects. Furthermore, the phenomenon of thermal quenching is explicitly correlated with the phonon frequency of the host matrix. Indeed, a higher phonon frequency would lead to a readily decreased emission intensity, ascribed as multi-phonon non-radiative relaxation [45].

Generally, temperature sensing based on the FIR technique involves the TCLs of particular Ln^{3+} ions, in which the phonon-assisted population shift takes place with the temperature rise [10,25,46]. Interestingly, two thermally coupled levels, $^1G_{4(1,2)}$ and $^3F_{2,3}/\ ^3H_4$, are commonly found in Tm^{3+} ions. Among them, the energy level $^1G_{4(1)}$ appears with remarkable intensity, while $^1G_{4(2)}$ does not show emission even with the increase in temperature [44]. Apart from that the noteworthy feature of TCLs, namely $^3F_{2,\ 3,}$ and $^3H_4$, exhibit a thermally dependent emission pattern as the temperature increases up to 480 K. Subsequently, the temperature quenching effect becomes more prominent causing the reduction of intensity, as seen in Fig. 11. Implementation of TCLs for temperature sensing using the FIR technique is regulated by Maxwell's Boltzmann relation and represented as follows [10,47]

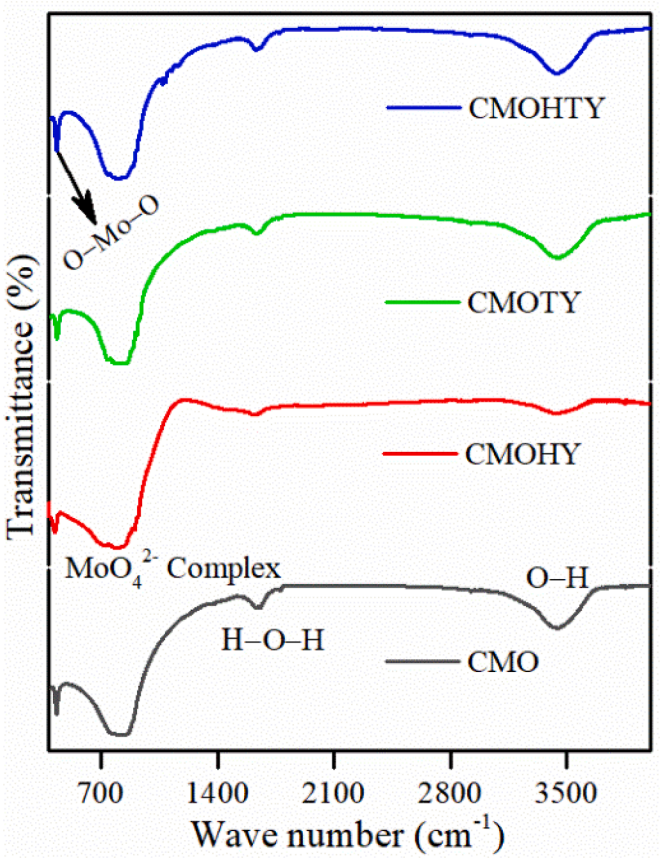

Fig. 6. FTIR spectra of CMO, CMOHY, CMOTY and CMOHTY phosphors calcined at 750 °C.

$$FIR = \frac{I_{20}}{I_{10}} = B \exp\left(-\frac{\Delta E}{kT}\right) \tag{3}$$

The value of absolute temperature can be calculated as follows

$$T = \frac{\Delta E}{k} \frac{1}{\ln\left(B/FIR\right)} \tag{4}$$

The parameters I_{20} and I_{10} represent the emission levels of thermally connected upper and lower excited states, respectively, with an energy gap ΔE. B represents an arbitrary constant, k signifies the Boltzmann constant, and T denotes the absolute temperature. The related parameter signifying the performance of the materials over a specified temperature range is usually divided into absolute sensitivity (S_a) and relative sensitivity (S_r) [47,48].

$$S_a = \frac{\partial FIR}{\partial T} = FIR\frac{\Delta E}{kT^2} \tag{5}$$

$$S_r = \frac{1}{FIR}\frac{\partial FIR}{\partial T} = \frac{\Delta E}{kT^2} \tag{6}$$

Where S_a is defined as the FIR variation with respect to temperature per kelvin (K^{-1}), mainly employed to compare the sensitivity of similar types of materials. Whereas the S_r is employed to quantify the percentage change of the FIR with respect to its own value for a temperature variation per Kelvin (K^{-1}) and is more general to compare across the different types of materials.

In the context of this phosphor material, the TCLs emission is relatively insignificant, while the emission commencing from NTCLs of Tm^{3+}/Ho^{3+} encompasses robust optical characteristics and demonstrates a remarkable temperature-dependent response across several emission bands [44]. For the different selected pair of NTCLs emission bands, namely I_{795}/I_{473}, I_{688}/I_{473}, I_{688}/I_{655}, and I_{688}/I_{795}, the traditional NTCLs-based FIR technique does not hold well, nevertheless, it is possible to establish the correlation between the FIR and the absolute temperature (T), which can be obtained by employing a plausible approximation based on the following equation [44,49]:

$$FIR = A_2 + \frac{A_2 - A_1}{1 + \exp\left(\frac{T - T_0}{Slope\ at\ T_0}\right)} \tag{7}$$

The function in discussion is typically known as the Boltzmann sigmoidal function [50]. It represents exponential growth with sinusoidal characteristics, which is entirely compatible with the shape of the NTCLs FIR plots. Where A_1 and A_2 are the initial and final values of the plot and the T_0 ($=\frac{A_1+A_2}{2}$) is defined as the mid value of the plot. The fitting result in Fig. 12 exhibits an excellent correlation with the experimental data. It is interesting to understand the process of FIR variation with temperature for the different pairs of NTCLs. In this particular case, the intensities of Tm^{3+} bands are comparatively higher than that of Ho^{3+} bands. The existence of thermally stimulated bands of Tm^{3+} ions, often known as thermionic emission, renders them advantageous for tracking temperatures. Close observation of all fittings initially shows slight variation with temperatures up to 400 K. At the same time, the FIR ratio significantly turns to a more significant value above this temperature, probably due to multi-phonon non-radiative relaxation not much prominent at this stage [45]. Above this, the emission bands in the high

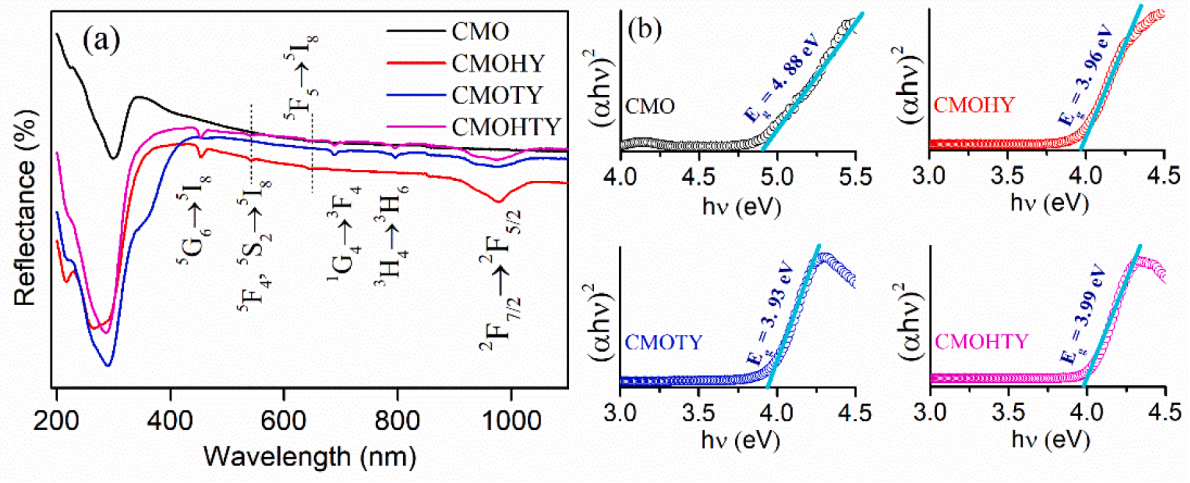

Fig. 7. (a) UV–Vis absorption spectra of CMO, CMOHY, CMOTY, and CMOHTY phosphor materials. **(b)** Tauc plot illustrating the bandgap of the same materials.

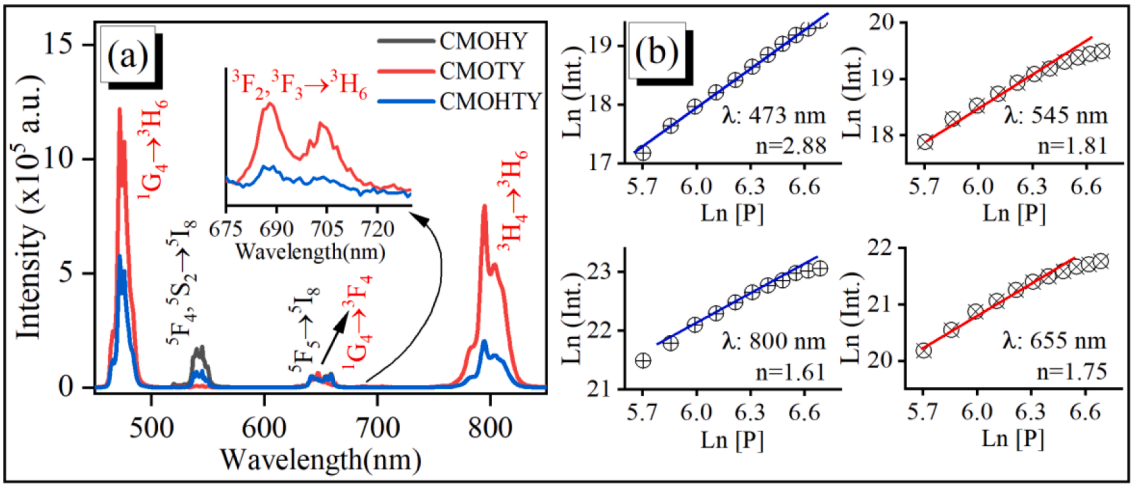

Fig. 8. **(a)** Upconversion spectra of the optimized CMOHY, CMOTY, and CMOHTY phosphor materials. **(b)** Ln-Ln plot corresponding to different emitting bands under 980 nm excitation.

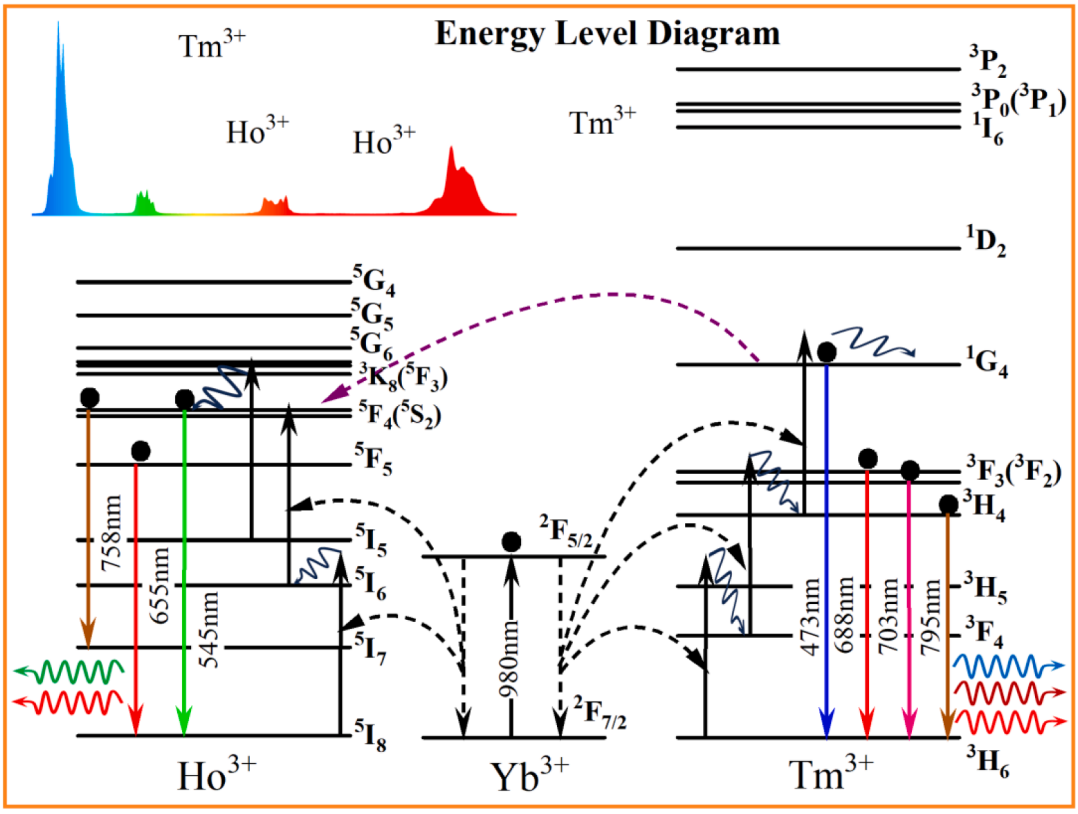

Fig. 9. Schematic energy level diagram of $Ho^{3+}/Tm^{3+}/Yb^{3+}$ ions with potential UC mechanisms.

energy side are effectively encountered with thermal de-excitation, along with an increase in thermionic emission situated at 688 nm. Subsequently, the comparison of sensitivity is calculated by estimating the sensitivity parameter S_a and S_r using the following equation [47].

$$S_a = \frac{\partial FIR}{\partial T} \text{ and } S_r = \frac{1}{FIR}\frac{\partial FIR}{\partial T} \quad (8)$$

The relevance of S_a and S_r, are already being discussed earlier. Fig. 13 exhibits the temperature sensitivity of different NTCLs groups, namely I_{795}/I_{473}, I_{688}/I_{473}, I_{688}/I_{655}, and I_{688}/I_{795}. A list of the absolute and relative sensitivity of different NTCLs groups is tabulated in Table 2. The highest absolute sensitivity value (S_a) was observed for the I_{795}/I_{473} at 500 K, which is 69.86×10^{-2} K^{-1}. In contrast, the values of S_a for the other NTCLs were comparatively more petite, with values of 0.614×10^{-2} K^{-1} at 455 K, 8.42×10^{-2} K^{-1} at 502 K, and 0.076×10^{-2} at 536 K for the I_{688}/I_{655}, I_{688}/I_{473}, and I_{688}/I_{795} respectively. In addition, the S_r value increases with temperature. It reaches its maximum values of 1.65 % K^{-1} and 3.01 % K^{-1} for the FIR ratio I_{795}/I_{473} and I_{688}/I_{473} at about 445 K and 435 K, respectively, subsequently exhibiting a declining tendency with temperature decrease. Meanwhile, the highest S_r values for I_{688}/I_{655} and I_{688}/I_{795} were observed at 303 K, corresponding to 18.57 % K^{-1} and 2.87 % K^{-1}, respectively. The higher relative sensitivity (S_r) associated with the I_{688}/I_{655} intensity ratio arises from the interplay between anti-thermal quenching of the Tm^{3+} ($^1G_4 \rightarrow {}^3F_{2,3}$ 688

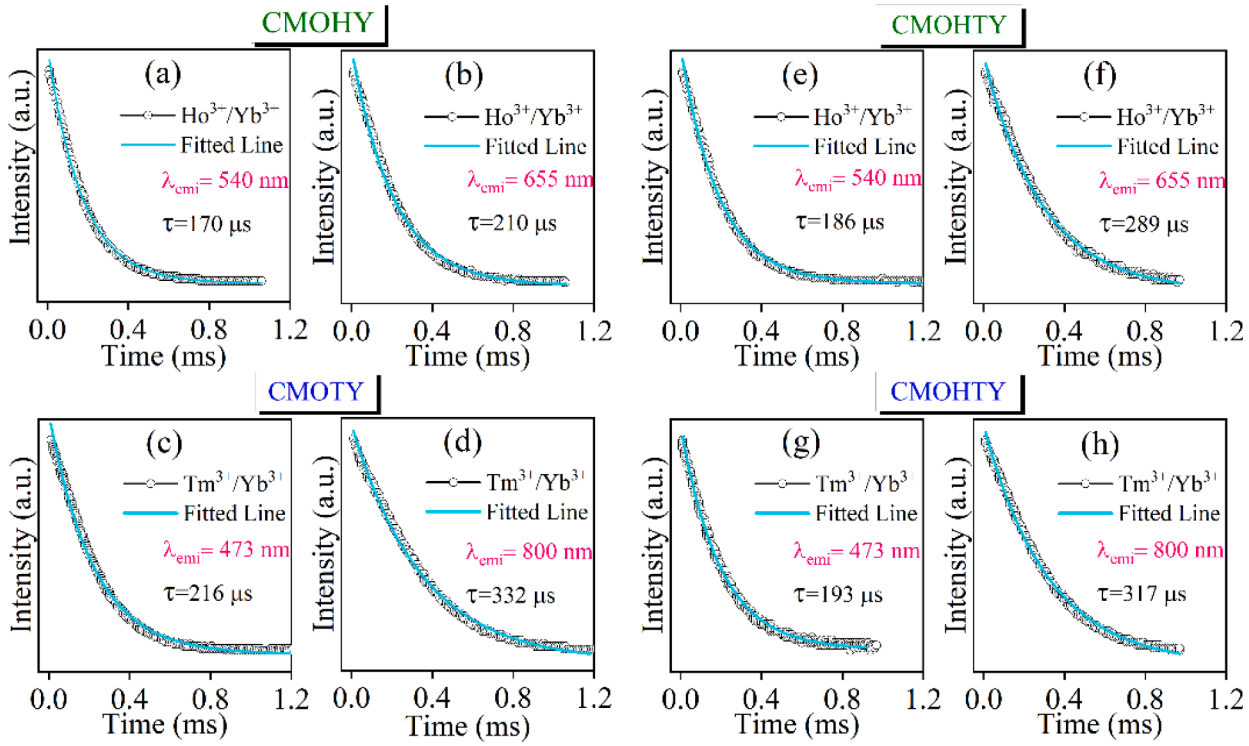

Fig. 10. Decay time analysis of different emitting bands i.e., (a-b) CMOHY (Ho^{3+} λ_{emi}=545 nm, 655 nm) and (c-d) CMOTY (λ_{emi}=473 nm, 795 nm), (e-f) CMOHTY (λ_{emi}=545 nm, 655 nm) and (g-h) (λ_{emi}=473 nm, 795 nm) under 980 nm excitation.

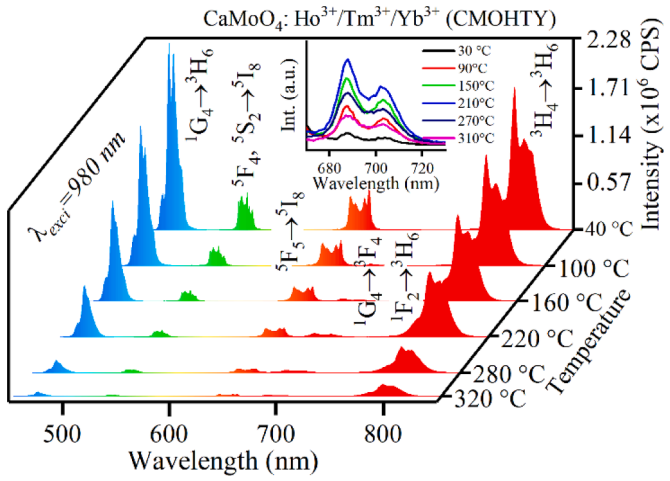

Fig. 11. Temperature-dependent UC emission of CMOHTY phosphors under 980 nm excitation.

nm) transition and conventional thermal quenching of the Ho^{3+} ($^5F_5 \rightarrow {}^5I_8$, 655 nm) emission at elevated temperatures. The contrasting thermal behaviours of these two emission levels result in a synergistic effect, which significantly enhances the thermal dependence of the I_{688}/I_{655} ratio [44].

Table 2 details the temperature sensitivity of phosphor materials based on the NTCLs of Ho^{3+}/Tm^{3+}. Notably, the $CaMoO_4$: $Ho^{3+}/Tm^{3+}/Yb^{3+}$ sample exhibits the highest S_a value for the I_{795}/I_{473} ratio (69.8 % K^{-1}) at 500 K, while the S_r value is most prominent for the I_{688}/I_{655} ratio (18.57 % K^{-1}) at 303 K, with the rest ratios ending up below those values. The study concludes that CMOHTY ($Ca_{0.89}Ho_{0.003}Tm_{0.007}Yb_{0.1}MoO_4$) phosphors exhibit robust temperature sensing capabilities based on NTCLs, with temperature-dependent solid responses and high sensitivity across multiple emission bands. Notably, this work reports for the first time the NTCLs-based temperature sensing in the $CaMoO_4$ host, along with the novel application of a Boltzmann sigmoidal fitting equation to model the FIR vs. temperature behaviour of NTCLs.

4.2. *Latent fingerprints (LFPs)*

As previously stated, the versatile optical properties of $Ho^{3+}/Tm^{3+}/Yb^{3+}$doped $CaMoO_4$ phosphor materials result in emission throughout the visible spectrum, with prominent emission for Tm^{3+} ions and relatively weak emission for Ho^{3+} ions. Furthermore, the individual emission can be easily distinguished by using a particular optical filter. Consequently, integrating fluorescent powder to visualise LFPs would be more intriguing due to the inherent exhibition of different colours in materials under NIR excitation. Generally, the most appropriate 'powder dusting' technique for acquiring LPFs on various substrates entails a specified set of detection processes [58]. In the dusting technique, the relevance of employed powder depends on adherence to an aqueous or oily substance on the substrate, allowing for clear visibility and definition of the latent print. Furthermore, the particle size, shape, relative surface area, and surface charge would also play a significant role. In conventional methods for detecting latent prints, UV lamps are commonly employed with various powders such as white or grey powder, fluorescent powder, magnetic powder, and black powder. These LFP powders are often composed of a specific pigment for good visibility, offering high contrast and resolution against background surfaces that clanged with an appropriate resilient carrier, as reported in multiple literature. The choice of powder depends on the surface type (substrate), such as porous, nonporous, coloured, and multitextured surfaces, as well as prevailing circumstances [59].

Herein, the $CaMoO_4$:$Ho^{3+}/Tm^{3+}/Yb^{3+}$ phosphor materials employed for latent fingerprinting through the 'dusting approach' have the advantage of capturing simultaneous coloured pictures due to their moisture affinity and propensity to cling to friction ridge skin residue without staining the substrate [60]. Intense blue, green, and red colours when subjected to near-infrared (NIR) excitation indicate the

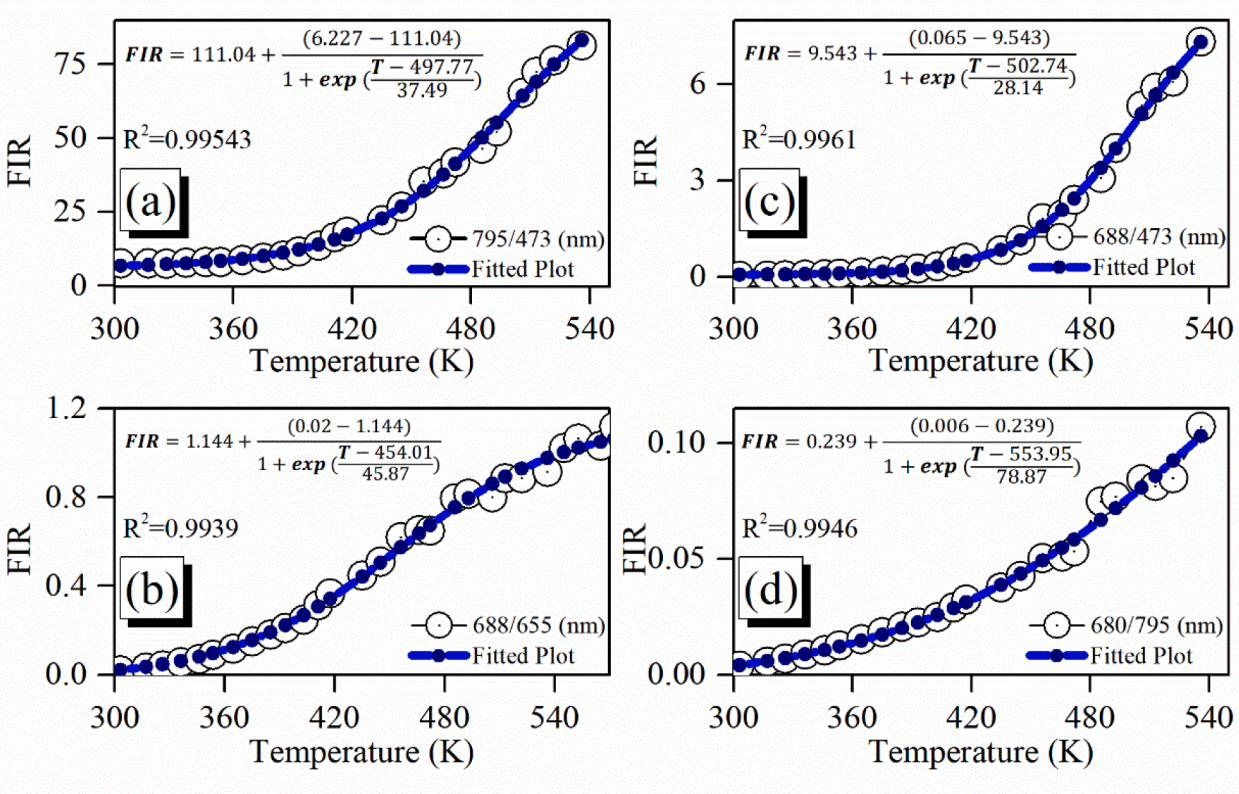

Fig. 12. FIR vs Temperature plots fitted with a Boltzmann sigmoidal function of different sets of NTCLs: (a) I_{795}/I_{473}, (b) I_{688}/I_{473}, (c) I_{688}/I_{655}, and (d) I_{688}/I_{795} of CMOHTY phosphors sample.

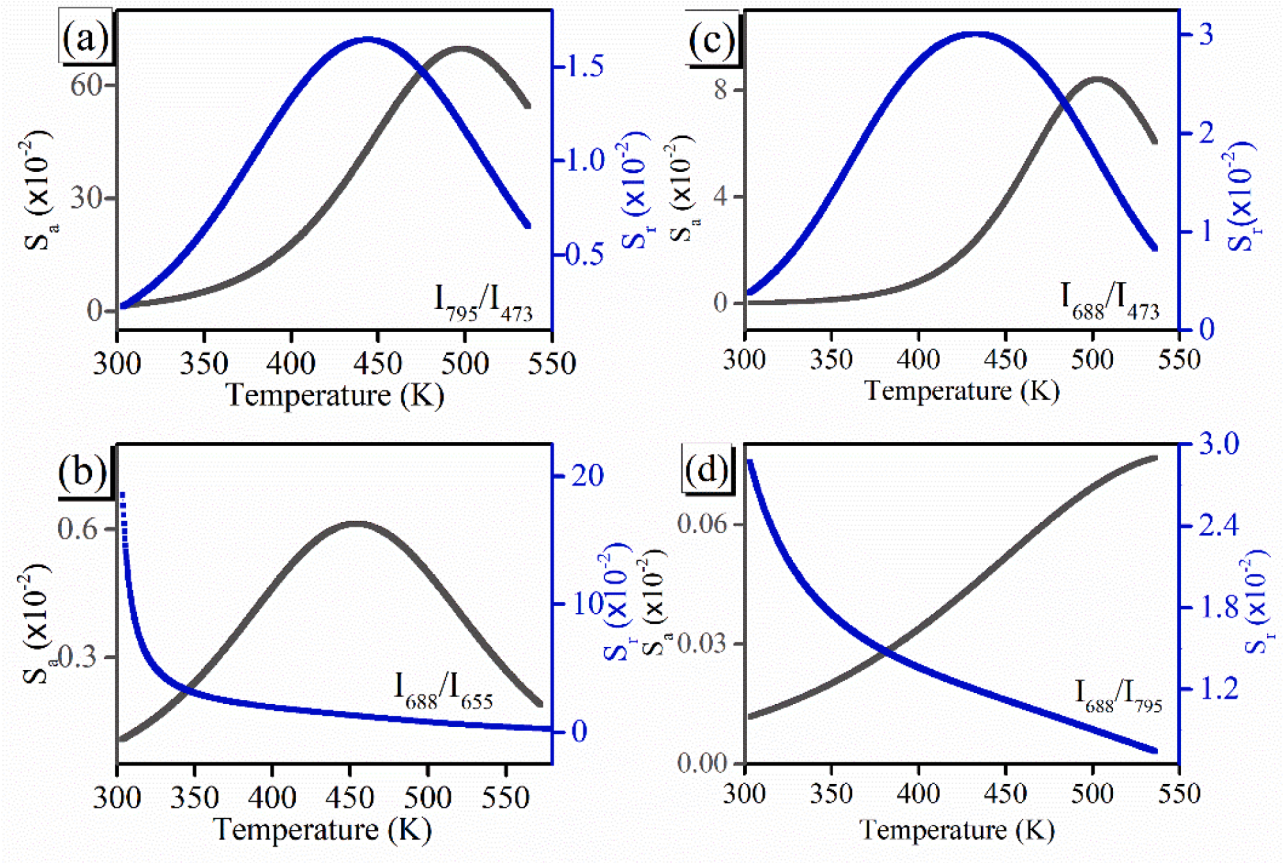

Fig. 13. Relative (S_r) and absolute sensitivity (S_a) plots for different sets of NTCLs, fitted to Boltzmann sigmoidal function.

Table 2
Comparison of temperature sensing characteristics based on FIR technique using NTCLs of Ho^{3+}/Tm^{3+} in various hosts with the involved transition.

Host: $Ho^{3+}/Tm^{3+}/Yb^{3+}$	I_1/I_2	Transitions	ΔE [cm^{-1}]	Max S_a [% K^{-1}]	Max S_r [% K^{-1}]	Refs.
$NaYF_4$	I_{696}/I_{541}	$^3F_3 \rightarrow {}^3H_6$ (Tm)/ $^5F_4 \rightarrow {}^5I_8$ (Ho)	3980	0.059 [495 K]	0.711 [320 K]	[44]
	I_{696}/I_{474}	$^3F_3 \rightarrow {}^3H_6$ (Tm)/$^1G_4 \rightarrow {}^3H_6$ (Tm)	6607	0.87 [495 K]	0.944 [445 K]	
	I_{696}/I_{522}	$^3F_3 \rightarrow {}^3H_6$ (Tm)/$^5F_3 \rightarrow {}^5I_8$ (Ho)	732	1.26 [495 K]	1.796 [345 K]	
	I_{696}/I_{644}	$^3F_3 \rightarrow {}^3H_6$ (Tm)/$^5F_5 \rightarrow {}^5I_8$ (Ho)	1956	0.057 [495 K]	0.955 [345 K]	
$BaIn_2O_4$	I_{795}/I_{480}	$^3F_4 \rightarrow {}^3H_6$ (Tm)/$^1G_4 \rightarrow {}^3H_6$ (Tm)	8563	25.45 [473 K]	1.48 [456 K]	[51]
	I_{795}/I_{550}	$^3H_4 \rightarrow {}^3H_6$ (Tm)/$^5F_4 \rightarrow {}^5I_8$ (Ho)	5603	1.83 [473 K]	0.48 [353 K]	
	I_{550}/I_{666}	$^5F_4 \rightarrow {}^5I_8$(Ho)/$^5F_5 \rightarrow {}^5I_8$ (Ho)	3167	3.32 [353 K]	0.44 [353 K]	
	I_{480}/I_{666}	$^1G_4 \rightarrow {}^3H_6$ (Tm)/$^5F_5 \rightarrow {}^5I_8$ (Ho)	5818	4.05 [353 K]	1.95 [473 K]	
	I_{550}/I_{480}	$^5F_4 \rightarrow {}^5I_8$ (Ho)/$^1G_4 \rightarrow {}^3H_6$ (Tm)	2651	4.89 [473 K]	1.19 [473 K]	
$Ba_3Y_4O_9$	I_{803}/I_{482}	$^3H_4 \rightarrow {}^3H_6$ (Tm)/$^1G_4 \rightarrow {}^3H_6$ (Tm)	8294	5.52 [575 K]	0.34 [575 K]	[49]
Y_2O_3	I_{477}/I_{488}	$^1G_4 \rightarrow {}^3H_6$ (Tm)/$^5F_3 \rightarrow {}^5I_8$ (Ho)	472	0.696 [303 K]	0.34 [303 K]	[52]
$NaLa(MoO_4)_2$	I_{695}/I_{545}	$^3F_3 \rightarrow {}^3H_6$ (Tm)/$^5F_4 \rightarrow {}^5I_8$ (Ho)	3960	2.848 [308 K]	1.63 [308 K]	[53]
$Gd_2(WO_3)_2$	I_{700}/I_{540}	$^3F_3 \rightarrow {}^3H_6$ (Tm)/$^5F_4 \rightarrow {}^5I_8$ (Ho)	4233	2.614 [595 K]	–	[54]
$KLu(WO_3)_2$	I_{696}/I_{545}	$^3F_3 \rightarrow {}^3H_6$ (Tm)/$^5F_4 \rightarrow {}^5I_8$ (Ho)	3980	–	0.60 [295 K]	[55]
Y_2SiO_5	I_{798}/I_{478}	$^3H_4 \rightarrow {}^3H_6$ (Tm)/$^1G_4 \rightarrow {}^3H_6$ (Tm)	8500	–	1.50 [298 K]	[56]
$NaYbF_4$	I_{803}/I_{477}	$^3H_4 \rightarrow {}^3H_6$ (Tm)/$^1G_4 \rightarrow {}^3H_6$ (Tm)	8511	28.44 [495 K]	0.66 [495 K]	[57]
$CaMoO_4$	I_{795}/I_{473}	$^3H_4 \rightarrow {}^3H_6$ (Tm)/$^1G_4 \rightarrow {}^3H_6$ (Tm)	8563	69.86 [500 K]	1.65 [445 K]	*Present Work
	I_{688}/I_{473}	$^1G_4 \rightarrow {}^3F_{2,3}$ (Tm)/$^1G_4 \rightarrow {}^3H_6$ (Tm)	6607	8.42 [502 K]	3.01 [435 K]	
	I_{688}/I_{655}	$^1G_4 \rightarrow {}^3F_{2,3}$ (Tm)/$^5F_5 \rightarrow {}^5I_8$ (Ho)	732	0.614 [455 K]	18.57 [303 K]	
	I_{688}/I_{795}	$^1G_4 \rightarrow {}^3F_{2,3}$ (Tm)/$^3H_4 \rightarrow {}^3H_6$ (Tm)	1956	0.08 [536 K]	2.87 [303 K]	

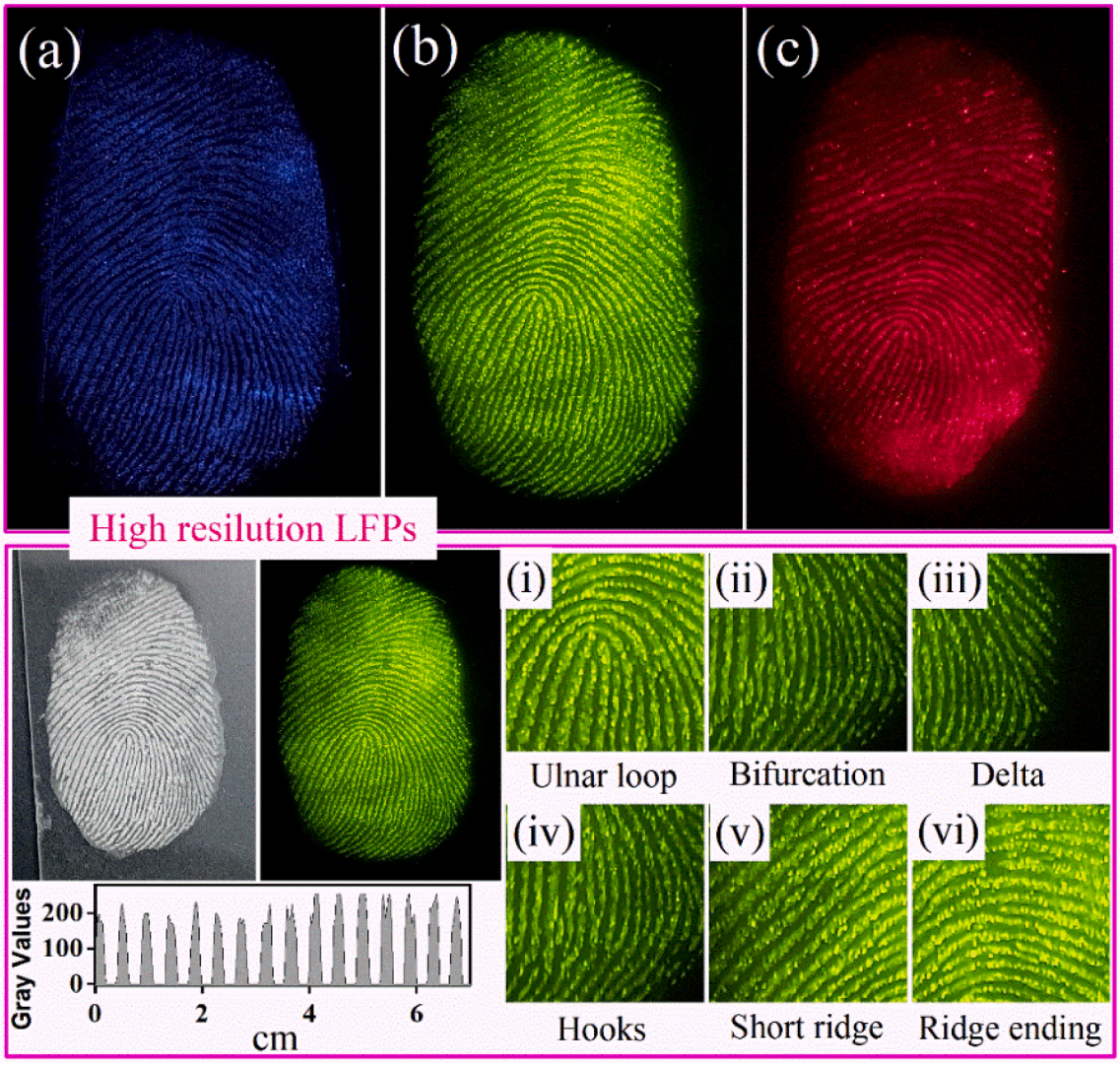

Fig. 14. (a-c) Coloured LFPs images were acquired using CMOHTY powder phosphors dusted over a glass plate substrate under 980 nm excitation, utilizing filters and high-resolution images of the green LFPs with various minutiae.

exceptional visibility of LFPs, which facilitates high contrast and adequate definition of prints as depicted, as shown in Fig. 14. The effectiveness of unique LFPs glow under NIR excitation to phosphors materials, created by friction ridges (raised) and furrows (recessed), resulting in cling to friction ridge skin residues such as organics (urea, creatinine, choline, amino acids, proteins, and so on) as well as inorganic salts secreted by glands (eccrine, apocrine, and sebaceous) through sweat pores. Generally, the distribution of ridge patterns, minutiae characteristics, ridge width and sweat pores are the main features employed to identify individual fingerprints, often categories in a hierarchical sequence. Fig. 14 shows a high-resolution coloured LFPs image of a volunteer acquired with consent with detailed information. The first recognition step involves identifying basic patterns such as loops, whorls, arches, etc. [61]. An ulnar loop pattern is found in the present case, as depicted in Fig. 14(i). The uniqueness of LFPs by examining the details of different numbers of minutiae and their related positions, categorized under second recognition steps, specifically including (ii) Bifurcation, (iii) Delta, (iv) Hooks, (v) short ridge, (vi) Ridge ending; demonstrated in high-resolution LFPs (Fig. 14). Ultimately, the ridge structure and its distinct properties, including the distribution of sweet pores (positioned centrally or peripherally on the ridges) and the curvature of the ridges, determine the authenticity and distinctiveness of individual LFPs. The typical ridge width ranges from 180 to 320 μm, and the average ridge intensity is almost uniform. Moreover, the scars found in prints may result from accidents, occupational activities, and ageing, which substantially aid in recognizing patterns; however, this is irrelevant in this case. In recent decades, predetermined computer algorithms have entirely replaced the traditional methods of understanding and reading the LFPs. These algorithms facilitate individual identification and allow for the creation of a reliable database. The acquisition of LFPs using the 'dusting method' with this developed fluorescent powder produces a clear and detailed image with excellent contrast and resolution compared to the surrounding surfaces. This ensures precise identification and enhances the reliability and validity of fingerprint analysis in forensic investigations [62].

5. Conclusion

This work accomplished the synthesis of Ho^{3+}/Yb^{3+}, Tm^{3+}/Yb^{3+} and $Ho^{3+}/Tm^{3+}/Yb^{3+}$ doped $CaMoO_4$ phosphors materials using hydrothermal technique through a hydrothermal method, subsequently undergoing post-calcination at 750 °C. Phase analysis confirms the formation of tetragonal structure of $CaMoO_4$, without any impurity peaks. The increase of particle size and their modification towards spherical then oval shape happens due to disparity in dopant valency, whereas the FTIR and UV–Vis investigation confirms the effective integration of dopant ions, evidenced by distinct vibrational modes and absorption bands, respectively. The strong UC emission and the underlying mechanism are supported by a power-dependent UC analysis. For temperature sensing, the different NTCL emission sets were analysed and fitted with a Boltzmann sigmoidal function, demonstrating the highest absolute sensitivity for the I_{795}/I_{473} (69.86×10^{-2} K^{-1} at 500 K). Additionally, $Ho^{3+}/Tm^{3+}/Yb^{3+}$ doped phosphors demonstrate excellent performance in LFPs imaging under NIR excitation, providing high contrast and clear visibility of ridge patterns for detailed fingerprint analysis. Overall, the findings of this research underscore the versatility and efficacy of $CaMoO_4$-based phosphors in both temperature sensing and forensic applications.

CRediT authorship contribution statement

Sachin Singh: Writing – original draft, Visualization, Software, Methodology, Investigation, Data curation. **Pradeep K. Vishwakarma:** Writing – review & editing, Validation, Investigation, Formal analysis, Data curation, Conceptualization. **Manisha Sharma:** Visualization, Validation, Formal analysis, Data curation. **Sunil K. Singh:** Writing – review & editing, Visualization, Validation, Supervision, Project administration, Formal analysis, Conceptualization.

Declaration of competing interest

The authors declare that they have no known competing financial interests or personal relationships that could have appeared to influence the work reported in this paper.

Acknowledgment

SKS is thankful to the SERB, Department of Science and Technology (DST), New Delhi, India, for the core research grant (CRG/2022/001393). Sachin Singh acknowledges the Department of Science and Technology (DST), Government of India, for providing the INSPIRE fellowship (IF180856).

Data availability

Data will be made available on request.

References

[1] Z. Gu, L. Yan, G. Tian, S. Li, Z. Chai, Y. Zhao, Recent advances in design and fabrication of upconversion nanoparticles and their safe theranostic applications, Adv. Mater. 25 (2013) 3758–3779.
[2] X. Qin, X. Liu, W. Huang, M. Bettinelli, X. Liu, Lanthanide-activated phosphors based on 4f-5d optical transitions: theoretical and experimental aspects, Chem. Rev. 117 (2017) 4488–4527.
[3] X. Wang, H. Chang, J. Xie, B. Zhao, B. Liu, S. Xu, W. Pei, N. Ren, L. Huang, W. Huang, Recent developments in lanthanide-based luminescent probes, Coord. Chem. Rev. 273 (2014) 201–212.
[4] M. Rai, S.K. Singh, K. Mishra, R. Shankar, R.K. Srivastava, S.B. Rai, Eu^{3+}-activated $CaGa_2O_4$ wide band gap (WBG) material for solar blind UV conversion: fluorescence and photo-conductivity performance, J. Mater. Chem. C 2 (2014) 7918–7926.
[5] W.J. Mir, T. Sheikh, H. Arfin, Z. Xia, A. Nag, Lanthanide doping in metal halide perovskite nanocrystals: spectral shifting, quantum cutting and optoelectronic applications, NPG Asia Mater. 12 (2020) 9.
[6] S.P. Panchangam, V.N.A. Naikan, Reliability analysis of temperature sensor system, Int. J. Reliab. Qual. Saf. Eng. 20 (2013) 1350003.
[7] M. Zhu, A thermometer based on diverse types thermocouples and resistance temperature detectors, J. Shanghai Jiaotong Univ. 20 (2015) 93–100.
[8] M.D. Dramićanin, Sensing temperature via downshifting emissions of lanthanide-doped metal oxides and salts. A review, Methods Appl. Fluoresc. 4 (2016) 42001.
[9] X. Wang, Q. Liu, Y. Bu, C.-S. Liu, T. Liu, X. Yan, Optical temperature sensing of rare-earth ion doped phosphors, RSC Adv. 5 (2015) 86219–86236.
[10] S. Singh, S. Kachhap, M. Sharma, S.K. Singh, Enhancing the temperature sensing property of a $Ca_{0.79-x}Bi_xEr_{0.01}Yb_{0.2}MoO_4$ phosphor via local symmetry distortion and reduction in non-radiative channels, RSC Adv. 13 (2023) 14991–15000.
[11] L. Li, Y. Cao, Y. Zhang, H. Cui, G. Li, J. Zhang, X. Zhang, B. Chen, Excellent upconversion luminescence intensity in $Er^{3+}/Yb^{3+}/Mo^{4+}$ triple-doped $BiTa_7O_{19}$ phosphors, J. Alloys Compd. 938 (2023) 168725.
[12] C. Wang, Y. Jin, R. Zhang, Q. Yao, Y. Hu, A review and outlook of ratiometric optical thermometer based on thermally coupled levels and non-thermally coupled levels, J. Alloys Compd. 894 (2022) 162494.
[13] M. Fhoula, M. Khitouni, M. Dammak, Comparative optical thermometry analysis using $Na_2SrP_2O_7$: Er^{3+}/Yb^{3+} phosphors: evaluation of LIR TCL and LIR NTCL methods for high-resolution temperature sensing, RSC Adv. 14 (2024) 39373–39380.
[14] P. Li, M. Jia, G. Liu, A. Zhang, Z. Sun, Z. Fu, Investigation on the fluorescence intensity ratio sensing thermometry based on nonthermally coupled levels, ACS Appl. Bio Mater. 2 (2019) 1732–1739.
[15] N. Zhang, H. Zhou, T. Wang, X. Ma, N. Lin, X. Fu, Y. Yin, J. Zhang, L. Ye, Z. Jia, High-sensitivity ratiometric thermometers of $Yb^{3+}/Er^{3+}/Tm^{3+}$ co-doped $LuScO_3$ single crystal fibers based on non-thermally coupled energy levels, J. Alloys Compd. 999 (2024) 174902.
[16] L.K. Bharat, G.S.R. Raju, J.S. Yu, Red and green colors emitting spherical-shaped calcium molybdate nanophosphors for enhanced latent fingerprint detection, Sci. Rep. 7 (2017) 1–14.
[17] F.K.F. Oliveira, M.C. Oliveira, L. Gracia, R.L. Tranquilin, C.A. Paskocimas, F. V. Motta, E. Longo, J. Andres, M.R.D. Bomio, Experimental and theoretical study to explain the morphology of $CaMoO_4$ crystals, J. Phys. Chem. Solids 114 (2018) 141–152.
[18] A.A. Ansari, A.K. Parchur, M. Alam, J. Labis, A. Azzeer, Influence of surface coating on structural and photoluminescent properties of $CaMoO_4$: Pr nanoparticles, J. Fluoresc. 24 (2014) 1253–1262.

[19] C. Bouzidi, K. Horchani-Naifer, Z. Khadraoui, H. Elhouichet, M. Ferid, Synthesis, characterization and DFT calculations of electronic and optical properties of $CaMoO_4$, Phys. B Condens. Matter 497 (2016) 34–38.

[20] R.S. Yadav, A. Rai, S.B. Rai, NIR light guided enhanced photoluminescence and temperature sensing in $Ho^{3+}/Yb^{3+}/Bi^{3+}$ co-doped $ZnGa_2O_4$ phosphor, Sci. Rep. 11 (2021) 4148.

[21] H. Guo, N. Dong, M. Yin, W. Zhang, L. Lou, S. Xia, Visible upconversion in rare earth ion-doped Gd_2O_3 nanocrystals, J. Phys. Chem. B 108 (2004) 19205–19209.

[22] S. Sinha, M.K. Mahata, H.C. Swart, A. Kumar, K. Kumar, Enhancement of upconversion, temperature sensing and cathodoluminescence in the K^+/Na^+ compensated $CaMoO_4$: er^{3+}/Yb^{3+} nanophosphor, New J. Chem. 41 (2017) 5362–5372.

[23] S. Gouraha, S. Sinha, A. Srivastava, J. Singh, Microwave assisted preparation of ternary scheelite $CaMoO_4$: Er^{3+}/Yb^{3+} nano-phosphors for up/down-conversion photoluminescence, temperature sensing and antibacterial properties, J. Photochem. Photobiol. A Chem. 458 (2025) 115967.

[24] R. Dey, V.K. Rai, Er^{3+}-Tm^{3+}-Yb^{3+}: $CaMoO_4$ phosphor as an outstanding upconversion-based optical temperature sensor and optical heater, Methods Appl. Fluoresc. 5 (2017) 15006.

[25] S. Singh, S. Kachhap, A.K. Singh, S. Pattnaik, S.K. Singh, Temperature sensing using bulk and nanoparticles of $Ca_{0.79}Er_{0.01}Yb_{0.2}MoO_4$ phosphor, Methods Appl. Fluoresc. 10 (2022) 44004.

[26] J. Bhagwan, S.K. Hussain, J.S. Yu, Facile hydrothermal synthesis and electrochemical properties of $CaMoO_4$ nanoparticles for aqueous asymmetric supercapacitors, ACS Sustain. Chem. Eng. 7 (2019) 12340–12350.

[27] A.I. Becerro, M. Allix, M. Laguna, D. González-Mancebo, C. Genevois, A. Caballero, G. Lozano, N.O. Núñez, M. Ocaña, Revealing the substitution mechanism in Eu^{3+}: $CaMoO_4$ and Eu^{3+}, Na^+: $CaMoO_4$ phosphors, J. Mater. Chem. C 6 (2018) 12830–12840.

[28] R.L. Tranquilin, L.X. Lovisa, C.R.R. Almeida, C.A. Paskocimas, M.S. Li, M. C. Oliveira, L. Gracia, J. Andres, E. Longo, F.V. Motta, Understanding the white-emitting $CaMoO_4$ Co-doped Eu^{3+}, Tb^{3+}, and Tm^{3+} phosphor through experiment and computation, J. Phys. Chem. C 123 (2019) 18536–18550.

[29] S. Sajwan, M. Sharma, S. Kachhap, M. Singhal, A.K. Singh, M. Tyagi, P.S. Sarkar, N. Chauhan, S.K. Singh, Structural and optical properties of $Zn_{2.95}Ga_{2-x}SnO_8$: xCr^{3+}: an excellent X-ray charging-based persistent phosphor, J. Alloys Compd. 978 (2024) 173405.

[30] K.C. Dubey, A. Zaidi, R.R. Awasthi, Environmentally benign structural, topographic, and sensing properties of pure and Al-doped ZnO thin films, ACS Omega 7 (2022) 28946–28954.

[31] V. Soleimanian, M. Saeedi, A. Mokhtari, The influence of heat treatment on the crystallite size, dislocation density, stacking faults probability and optical band gap of nanostructured cadmium sulfide films, Mater. Sci. Semicond. Process. 30 (2015) 118–127.

[32] P.K. Vishwakarma, S.B. Rai, A. Bahadur, Enhanced green up/down-conversion emissions through phase transformation in Ho^{3+}/Yb^{3+} co-doped Y_2O_3: ZrO_2 phosphors in presence of Na^+ ions, Opt. Mater. (Amst). 139 (2023) 113814.

[33] N. Kaczorowska, A. Szczeszak, W. Nowicki, S. Lis, A new synthesis approach for upconverting nanoparticles based on rare earth ternary vanadates, Ceram. Int. 46 (2020) 26309–26316.

[34] M. Guo, J. Lu, Y. Wu, Y. Wang, M. Luo, UV and visible Raman studies of oxygen vacancies in rare-earth-doped ceria, Langmuir 27 (2011) 3872–3877.

[35] V.M. Longo, L.S. Cavalcante, E.C. Paris, J.C. Sczancoski, P.S. Pizani, M.S. Li, J. Andrés, E. Longo, J.A. Varela, Hierarchical assembly of $CaMoO_4$ nano-octahedrons and their photoluminescence properties, J. Phys. Chem. C 115 (2011) 5207–5219.

[36] G. Botelho, I.C. Nogueira, E. Moraes, E. Longo, Study of structural and optical properties of $CaMoO_4$ nanoparticles synthesized by the microwave-assisted solvothermal method, Mater. Chem. Phys. 183 (2016) 110–120.

[37] T. Tsuboi, K. Shimamura, Up-conversion processes in Ho^{3+}/Tm^{3+}-codoped $LiYF_4$ crystals. Solid State Lasers and Amplifiers, SPIE, 2004, pp. 187–194.

[38] M. Luo, X. Sha, B. Chen, X. Zhang, H. Yu, X. Li, J. Zhang, S. Xu, Y. Cao, Y. Wang, Optical transition properties, internal quantum efficiencies, and temperature sensing of Er^{3+} doped $BaGd_2O_4$ phosphor with low maximum phonon energy, J. Am. Ceram. Soc. 105 (2022) 3353–3363.

[39] N. Rakov, G.S. Maciel, A study of energy transfer phenomenon leading to photon up-conversion in Ho^{3+}: Yb^{3+}: CaF_2 crystalline powders and its temperature sensing properties, Curr. Appl. Phys. 17 (2017) 1223–1231.

[40] K. Hoang, Rare-earth defects in GaN: a systematic investigation of the lanthanide series, Phys. Rev. Mater. 6 (2022) 44601.

[41] P. Guo, J. Wang, C. Liao, H. Zhou, D. Huang, G. Zhou, X. Yu, J. Hu, Luminescence, energy transfer, colour modulation and up-conversion mechanisms of Yb^{3+}, Tm^{3+} and Ho^{3+} co-doped Y_6MoO_{12}, RSC Adv. 12 (2022) 33419–33428.

[42] M. Sedano, S. Babu, R. Balda, J. Fernández, A. Durán, M.J. Pascual, Spark plasma sintering and optical properties of Tm^{3+} and Tm^{3+}/Yb^{3+} doped $NaLaF_4$ transparent glass-ceramics, J. Alloys Compd. 948 (2023) 169552.

[43] H. Guan, G. Liu, J. Wang, X. Dong, W. Yu, Tunable color and energy transfer of Tm^{3+} and Ho^{3+} co-doped $NaGdF_4$ nanoparticles, RSC Adv. 5 (2015) 50611–50616.

[44] Z. Cheng, M. Meng, J. Wang, Z. Li, J. He, H. Liang, X. Qiao, Y. Liu, J. Ou, High-sensitivity $NaYF_4$: $Yb^{3+}/Ho^{3+}/Tm^{3+}$ phosphors for optical temperature sensing based on thermally coupled and non-thermally coupled energy levels, Nanoscale 15 (2023) 11179–11189.

[45] J. Zhang, Y. Zhang, X. Jiang, Investigations on upconversion luminescence of $K_3Y(PO_4)_2$: Yb^{3+}-$Er^{3+}/Ho^{3+}/Tm^{3+}$ phosphors for optical temperature sensing, J. Alloys Compd. 748 (2018) 438–445.

[46] Y. Yu, K. Li, M. Dai, H. Xu, Y. Wei, R. Wang, Z. Fu, Toward ultra-high sensitivity optical thermometers and bright yellow LEDs based on phonon-assisted energy transfer in rare earth-doped La_2ZnTiO_6 double perovskite, Inorg. Chem. 63 (2024) 14142–14151.

[47] D. Gao, B. Chen, X. Sha, Y. Zhang, X. Chen, L. Wang, X. Zhang, J. Zhang, Y. Cao, Y. Wang, Near infrared emissions from both high efficient quantum cutting (173%) and nearly-pure-color upconversion in $NaY(WO_4)_2$: Er^{3+}/Yb^{3+} with thermal management capability for silicon-based solar cells, Light Sci. Appl. 13 (2024) 17.

[48] H. Cui, Y. Cao, Y. Zhang, L. Cao, S. Ran, X. Wang, D. Wu, X. Li, X. Zhang, B. Chen, Extremely intense green up-conversion luminescent and ultra-high temperature sensitivity in Er^{3+}/Yb^{3+} co-doped $BiTa_7O_{19}$ phosphors, J. Lumin. 241 (2022) 118484.

[49] S. Liu, J. Cui, J. Jia, J. Fu, W. You, Q. Zeng, Y. Yang, X. Ye, High sensitive $In^{3+}/Tm^{3+}/Yb^{3+}$ (In^{3+}= Ho^{3+}, Er^{3+}) tri-doped $Ba_3Y_4O_9$ upconverting optical thermometric materials based on diverse thermal response from non-thermally coupled energy levels, Ceram. Int. 45 (2019) 1–10.

[50] K. Heusser, R. Heusser, J. Jordan, V. Urechie, A. Diedrich, J. Tank, Baroreflex curve fitting using a WYSIWYG boltzmann sigmoidal equation, Front. Neurosci. 15 (2021) 697582.

[51] H. Liu, M. Liu, K. Wang, B. Wang, X. Jian, G. Bai, Y. Zhang, Efficient upconversion emission and high-sensitivity thermometry of $BaIn_2O_4$: $Yb^{3+}/Tm^{3+}/RE^{3+}$(RE= Er^{3+}, Ho^{3+}) phosphor, Dalt. Trans. 50 (2021) 12107–12117.

[52] A. Pandey, V.K. Rai, Optical thermometry using FIR of two close lying levels of different ions in Y_2O_3: Ho^{3+}–Tm^{3+}–Yb^{3+} phosphor, Appl. Phys. B 113 (2013) 221–225.

[53] S. Tomar, N.K. Mishra, V. Chauhan, K. Kumar, C. Shivakumara, Strategic investigation of dual-mode light emission from $Tm^{3+}/Ho^{3+}/Yb^{3+}$-activated $NaLa(MoO_4)_2$ phosphors for color tunability and optical temperature sensing applications, J. Phys. Chem. C 128 (24) (2024) 10159–10174.

[54] H. Lu, H. Hao, Y. Gao, D. Li, G. Shi, Y. Song, Y. Wang, X. Zhang, Optical sensing of temperature based on non-thermally coupled levels and upconverted white light emission of a $Gd_2(WO_4)_3$ phosphor co-doped with in Ho (III), Tm (III), and Yb (III), Microchim. Acta 184 (2017) 641–646.

[55] O.A. Savchuk, J.J. Carvajal, M.C. Pujol, J. Massons, P. Haro-González, O. Martínez, J. Jiménez, M. Aguiló, F. Díaz, New strategies invonving upconverting nanoparticles for determining moderate temperatures by luminescence thermometry, J. Lumin. 169 (2016) 711–716.

[56] N. Rakov, Tm^{3+}, Yb^{3+}: Y_2SiO_5 up-conversion phosphors: exploration of temperature sensing performance by monitoring the luminescence emission, Phys. B Condens. Matter 628 (2022) 413572.

[57] Z. Cheng, J. Lu, Z. Li, M. Meng, X. Qiao, Y. Liu, J. Ou, Promising lanthanide-$NaYbF_4$: Er^{3+}@ $NaYbF_4$: Tm^{3+} micro-phosphors for highly efficient upconversion luminescence and temperature sensing, Opt. Mater. (Amst). 154 (2024) 115675.

[58] A.A. Ansari, K.M. Aldajani, A.N. AlHazaa, H.A. Albrithen, Recent progress of fluorescent materials for fingermarks detection in forensic science and anti-counterfeiting, Coord. Chem. Rev. 462 (2022) 214523.

[59] G.R. Mamatha, B.R.R. Krushna, J. Malleshappa, B. Subramanian, B.D. Prasad, C. Srikanth, H. Nagabhushana, Designing orange-red emitting luminescent platform for data security and information encryption based Sm^{3+} doped BLAO phosphor, J. Photochem. Photobiol. A Chem. 439 (2023) 114560.

[60] P. Gayathri, S.B. Subramaniyan, A. Veerappan, M. Pannipara, A.G. Al-Sehemi, D. Moon, S.P. Anthony, Knotting two donor− π-acceptor AIEgens using a nonconjugated linker: tunable and switchable fluorescence and fingerprinting and live cell imaging applications, Cryst. Growth Des. 22 (2021) 633–642.

[61] J. Lee, C.W. Lee, J.-M. Kim, A magnetically responsive polydiacetylene precursor for latent fingerprint analysis, ACS Appl. Mater. Interfaces 8 (2016) 6245–6251.

[62] Q. Zhu, W. Wang, G. Sun, A.A. Aryee, J. Wei, H. Meng, W. Kong, Z. Li, Red emissive nanocomposite with high quantum yield for ultrasensitive and selective detection of latent fingerprints, Microchem. J. 190 (2023) 108688.